A Discontinuous Galerkin Solver for Boltzmann Poisson Systems in Nano Devices

Chi-Wang Shu

Division of Applied Mathematics

Brown University

Joint work with Yingda Cheng, Irene M. Gamba and Armando Majorana

Outline

- Introduction to the discontinuous Galerkin (DG) method for hyperbolic equations with source terms and for elliptic equations
- A DG solver for the Boltzmann-Poisson systems in nano devices
- Simulation results
- Conclusions and future work

Introduction to the DG method

DG method for hyperbolic equations with source terms

To solve a hyperbolic conservation law with a source term:

$$u_t + f(u)_x = g(u, x) \tag{1}$$

Multiplying with a test function v, integrate over a cell $I_j = [x_{j-\frac{1}{2}}, x_{j+\frac{1}{2}}]$, and integrate by parts:

$$\int_{I_j} u_t v dx - \int_{I_j} f(u) v_x dx + f(u_{j+\frac{1}{2}}) v_{j+\frac{1}{2}} - f(u_{j-\frac{1}{2}}) v_{j-\frac{1}{2}} = \int_{I_j} g(u, x) v dx$$

Now assume both the solution u and the test function v come from a finite dimensional approximation space V_h, which is usually taken as the space of piecewise polynomials of degree up to k:

$$V_h = \left\{ v : v|_{I_j} \in P^k(I_j),\ j = 1, \cdots, N \right\}$$

However, the boundary terms $f\left(u_{j+\frac{1}{2}}\right)$, $v_{j+\frac{1}{2}}$ etc. are not well defined when u and v are in this space, as they are discontinuous at the cell interfaces.

From the conservation and stability (upwinding) considerations, we take

- A single valued monotone numerical flux to replace $f(u_{j+\frac{1}{2}})$:

$$\hat{f}_{j+\frac{1}{2}} = \hat{f}(u^-_{j+\frac{1}{2}}, u^+_{j+\frac{1}{2}})$$

where $\hat{f}(u,u) = f(u)$ (consistency); $\hat{f}(\uparrow,\downarrow)$ (monotonicity) and $\hat{f}$ is Lipschitz continuous with respect to both arguments.

For simple linear equations, $f(u) = a(x)u$ with a given function $a(x)$, the upwind flux is fine:

$$\hat{f}_{j+\frac{1}{2}} = \begin{cases} a(x_{j+\frac{1}{2}}) f(u^-_{j+\frac{1}{2}}), & \text{if } a(x_{j+\frac{1}{2}}) \geq 0 \\ a(x_{j+\frac{1}{2}}) f(u^+_{j+\frac{1}{2}}), & \text{if } a(x_{j+\frac{1}{2}}) < 0 \end{cases}$$

- Values from inside I_j for the test function v

$$v^-_{j+\frac{1}{2}}, \qquad v^+_{j-\frac{1}{2}}$$

Hence the DG scheme is: find $u \in V_h$ such that

$$\int_{I_j} u_t v dx - \int_{I_j} f(u) v_x dx + \hat{f}_{j+\frac{1}{2}} v^-_{j+\frac{1}{2}} - \hat{f}_{j-\frac{1}{2}} v^+_{j-\frac{1}{2}} = \int_{I_j} g(u,x) v dx \tag{2}$$

for all $v \in V_h$.

Time discretization could be by the TVD Runge-Kutta method (Shu and Osher, JCP 88). For the semi-discrete scheme:

$$\frac{du}{dt} = L(u)$$

where $L(u)$ is a discretization of the spatial operator, the third order TVD Runge-Kutta is simply:

$$\begin{aligned} u^{(1)} &= u^n + \Delta t L(u^n) \\ u^{(2)} &= \frac{3}{4}u^n + \frac{1}{4}u^{(1)} + \frac{1}{4}\Delta t L(u^{(1)}) \\ u^{n+1} &= \frac{1}{3}u^n + \frac{2}{3}u^{(2)} + \frac{2}{3}\Delta t L(u^{(2)}) \end{aligned}$$

DG method for elliptic equations. The simple example

$$-u_{xx} = f(x), \qquad 0 < x < 1$$

$$u(0) = a, \qquad u_x(1) = b$$

Several classes of DG schemes are available. We use the local DG (LDG) scheme. That is, rewrite the equation as

$$-p_x = f(x), \qquad u_x = p.$$

Then write the LDG scheme as: find $u, p \in V_h$ such that

$$\int_{I_j} pq_x dx - \hat{p}_{j+\frac{1}{2}} q^-_{j+\frac{1}{2}} + \hat{p}_{j-\frac{1}{2}} q^+_{j-\frac{1}{2}} = \int_{I_j} fq dx,$$

$$-\int_{I_j} uv_x dx + \hat{u}_{j+\frac{1}{2}} v^-_{j+\frac{1}{2}} - \hat{u}_{j-\frac{1}{2}} v^+_{j-\frac{1}{2}} = \int_{I_j} pv dx,$$

for all $v, q \in V_h$.

The crucial point here is still the choice of the numerical fluxes $\hat{u}_{j+\frac{1}{2}}$ and $\hat{p}_{j+\frac{1}{2}}$. For the boundary condition in this simple example, it suffices to take the alternating flux choice

$$\hat{u}_{j+\frac{1}{2}} = u^-_{j+\frac{1}{2}}, \qquad \hat{p}_{j+\frac{1}{2}} = p^+_{j+\frac{1}{2}}.$$

Advantages of the DG method:

- Easy handling of complicated geometry and boundary conditions (common to all finite element methods). Allowing hanging nodes in the mesh;
- Compact. Communication only with immediate neighbors, regardless of the order of the scheme;
- Explicit. Because of the discontinuous basis, the mass matrix is local to the cell, resulting in explicit time stepping (no systems to solve);
- Parallel efficiency. Achieves 99% parallel efficiency for static mesh and over 80% parallel efficiency for dynamic load balancing with adaptive meshes (Flaherty et al.);

- Provable cell entropy inequality and L^2 stability, for arbitrary scalar equations in any spatial dimension and any triangulation, for any order of accuracy, without limiters;
- At least ($k + \frac{1}{2}$)-th order accurate, and often ($k + 1$)-th order accurate for smooth solutions when piecewise polynomials of degree k are used, regardless of the structure of the meshes.
- Easy h-p adaptivity.
- Stable and convergent DG methods are now available for many nonlinear PDEs containing higher derivatives: convection diffusion equations, KdV equations, ...

An example

We show an example to demonstrate the excellent performance of the DG method.

Consider the linear convection equation

$$u_t + u_x = 0, \qquad or \qquad u_t + u_x + u_y = 0,$$

on the domain $(0, 2\pi) \times (0, T)$ or $(0, 2\pi)^2 \times (0, T)$ with the characteristic function of the interval $(\frac{\pi}{2}, \frac{3\pi}{2})$ or the square $(\frac{\pi}{2}, \frac{3\pi}{2})^2$ as initial condition and periodic boundary conditions.

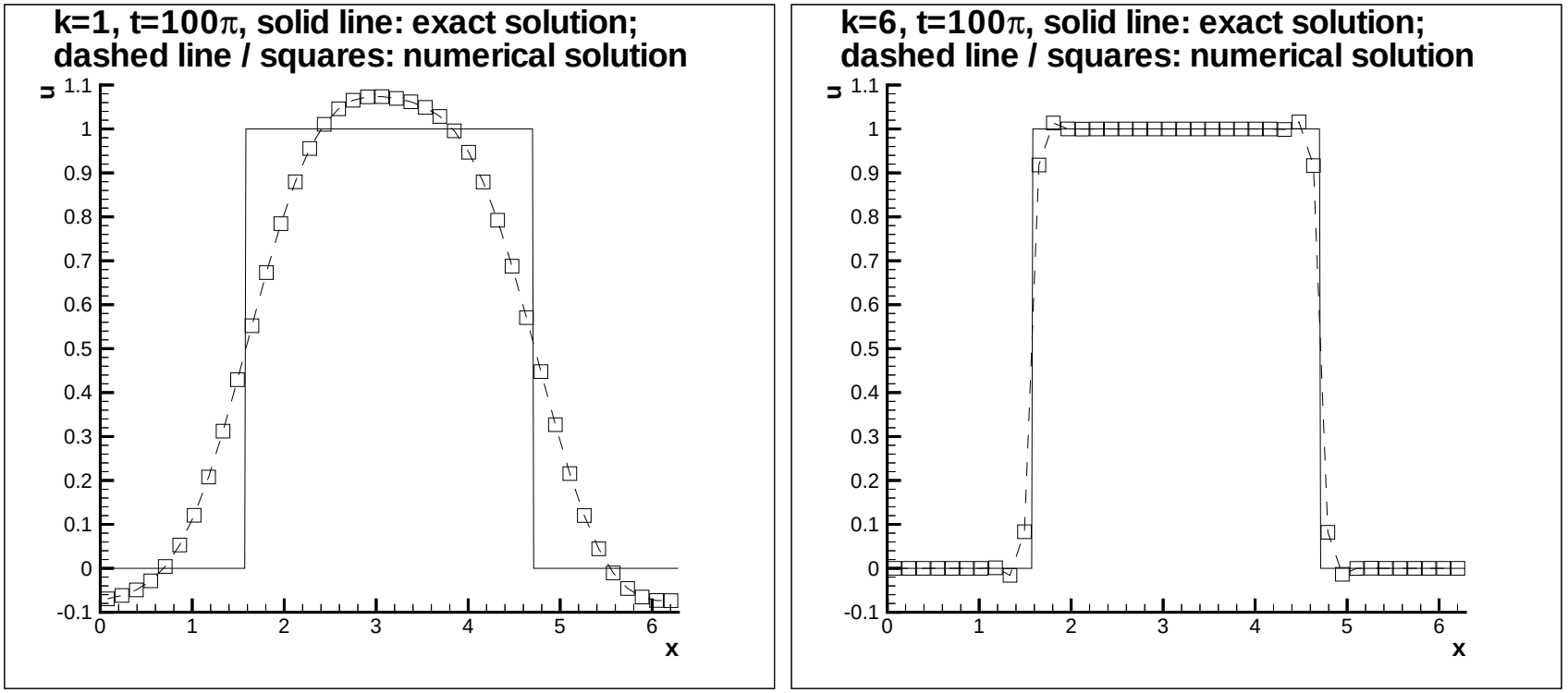

Figure 1: Transport equation: Comparison of the exact and the RKDG solutions at $T = 100\pi$ with second order (P^1, left) and seventh order (P^6, right) RKDG methods. One dimensional results with 40 cells, exact solution (solid line) and numerical solution (dashed line and symbols, one point per cell)

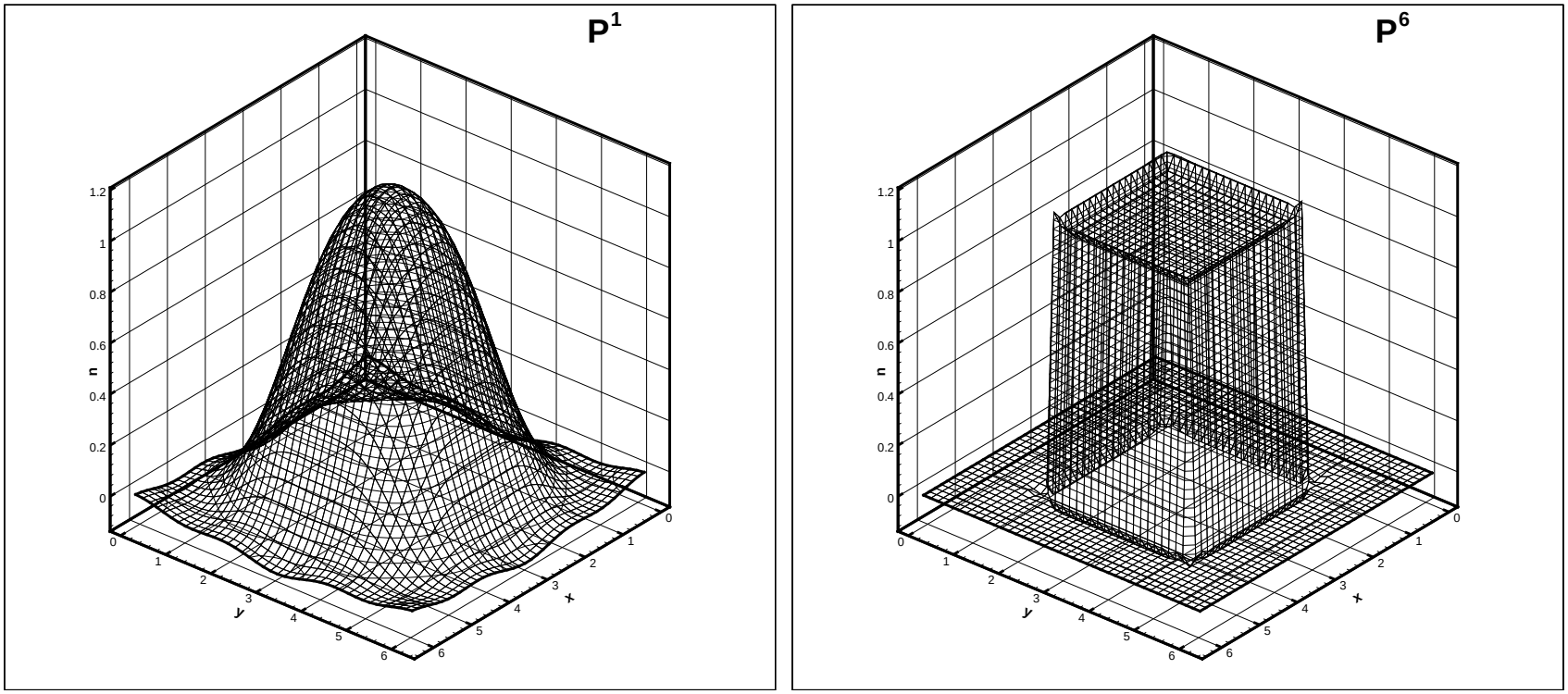

Figure 2: Transport equation: Comparison of the exact and the RKDG solutions at $T = 100\pi$ with second order (P^1, left) and seventh order (P^6, right) RKDG methods. Two dimensional results with 40×40 cells.

History of the DG method:

Here is a (very incomplete) history of the study of DG methods:

- 1973: First discontinuous Galerkin method for steady state linear scalar conservation laws (Reed and Hill).
- 1974: First error estimate (for tensor product mesh) of the discontinuous Galerkin method of Reed and Hill (LeSaint and Raviart).
- 1986: Error estimates for discontinuous Galerkin method of Reed and Hill (Johnson and Pitkäranta).
- 1989-1998: Runge-Kutta discontinuous Galerkin method for *nonlinear* conservation laws (Cockburn, Shu, ...).

- 1994: Proof of cell entropy inequality for discontinuous Galerkin method for nonlinear conservation laws in general multidimensional triangulations (Jiang and Shu).
- 1997-1998: Discontinuous Galerkin method for convection diffusion problems (Bassi and Rebay, Cockburn and Shu, Baumann and Oden, ...).
- 2002: Discontinuous Galerkin method for partial differential equations with third or higher order spatial derivatives (KdV, biharmonic, ...) (Yan and Shu, Xu and Shu, ...)

Collected works and books on the DG methods:

- Discontinuous Galerkin Methods: Theory, Computation and Applications, B. Cockburn, G. Karniadakis and C.-W. Shu, editors, Lecture Notes in Computational Science and Engineering, volume 11, Springer, 2000. (Proceedings of the first DG Conference)
- Journal of Scientific Computing, special issue on DG methods, 2005.
- Computer Methods in Applied Mechanics and Engineering, special issue on DG methods, 2006.
- Four recent books on DG methods: Hesthaven and Warburton; Kanschat; Li; and Riviere.

A DG solver for the Boltzmann Poisson Systems

The electron distribution function $f(\mathrm{t}, \mathbf{x}, \mathbf{k})$ in semiconductors in dependence of time t, position $\mathbf{x}$ and electron wave vector $\mathbf{k}$ is governed by the Boltzmann transport equation (BTE)

$$\frac{\partial f}{\partial \mathrm{t}} + \frac{1}{\hbar}\nabla_{\mathbf{k}}\,\varepsilon \cdot \nabla_{\mathbf{x}} f - \frac{q}{\hbar}\mathbf{E} \cdot \nabla_{\mathbf{k}} f = Q(f)\,, \tag{3}$$

where

- $\hbar$ is the reduced Planck constant
- q denotes the positive elementary charge

- The function $\varepsilon(\mathbf{k})$ is the energy of the considered crystal conduction band measured from the band minimum; according to the Kane dispersion relation, ε is the positive root of

$$\varepsilon(1+\alpha\varepsilon) = \frac{\hbar^2 k^2}{2m^*}\,, \tag{4}$$

where α is the non-parabolicity factor and m^* the effective electron mass.

- The electric field $\mathbf{E}$ is related to the doping density N_D and the electron density n (the zero-order moment of the electron distribution function f), by the Poisson equation

$$\nabla_{\mathbf{x}} \left[\epsilon_r(\mathbf{x}) \nabla_{\mathbf{x}} V\right] = \frac{q}{\epsilon_0} \left[n(\mathrm{t}, \mathbf{x}) - N_D(\mathbf{x})\right], \quad \mathbf{E} = -\nabla_{\mathbf{x}} V \,, \quad (5)$$

where ϵ_0 is the dielectric constant of the vacuum, $\epsilon_r(\mathbf{x})$ labels the relative dielectric function depending on the material and V the electrostatic potential.

- The collision operator $Q(f)$ takes into account acoustic deformation potential and optical intervalley scattering. For low electron densities, it reads

$$Q(f)(\mathrm{t},\mathbf{x},\mathbf{k}) = \int_{\mathbb{R}^3} \left[S(\mathbf{k}',\mathbf{k}) f(\mathrm{t},\mathbf{x},\mathbf{k}') - S(\mathbf{k},\mathbf{k}') f(\mathrm{t},\mathbf{x},\mathbf{k})\right] d\mathbf{k}' \tag{6}$$

with the scattering kernel

$$\begin{aligned} S(\mathbf{k},\mathbf{k}') \;=\; & (n_q+1)\, K\, \delta(\varepsilon(\mathbf{k}') - \varepsilon(\mathbf{k}) + \hbar\omega_p) \\ & + n_q\, K\, \delta(\varepsilon(\mathbf{k}') - \varepsilon(\mathbf{k}) - \hbar\omega_p) + K_0\, \delta(\varepsilon(\mathbf{k}') - \varepsilon(\mathbf{k})) \end{aligned}$$

and K and K_0 being constant for silicon. The symbol δ indicates the usual Dirac distribution and ω_p is the constant phonon frequency.

We note that

- The Boltzmann-Poisson system is an equation in six dimensions (plus time if the device is not in steady state) for a truly 3-D device, five dimensions for a 2-D device, and four dimensions for a 1-D device.
- This heavy computational cost explains why the BP system is traditionally simulated by the Direct Simulation Monte Carlo (DSMC) methods.
- In recent years, deterministic solvers to the BP system were proposed. These methods provide accurate results which, in general, agree well with those obtained from Monte Carlo (DSMC) simulations, often at a fractional computational time. Moreover, they can resolve transient details for the *pdf*, which are difficult to compute with DSMC simulators.

- Weighted essentially non-oscillatory (WENO) finite difference schemes were used to solve the Boltzmann-Poisson system (Carrillo, Gamba, Majorana and Shu, JCP03, 06). The advantage of the WENO scheme is that it is relatively simple to code and very stable even on coarse meshes for solutions containing sharp gradient regions. A disadvantage of the WENO finite difference method is that it requires smooth meshes to achieve high order accuracy, hence it is not very flexible for adaptive meshes.

We first introduce suitable dimensionless quantities and variables, and then perform a coordinate transformation for $\mathbf{k}$ according to

$$\mathbf{k} = \frac{\sqrt{2m^* k_B T_L}}{\hbar} \sqrt{w(1+\alpha_K w)} \left(\mu, \sqrt{1-\mu^2}\cos\varphi, \sqrt{1-\mu^2}\sin\varphi \right), \tag{7}$$

where the new independent variables are the dimensionless energy $w = \dfrac{\varepsilon}{k_B T_L}$, the cosine of the polar angle μ and the azimuth angle φ with $\alpha_K = k_B T_L \alpha$.

The main advantage of the generalized spherical coordinates (7) is the easy treatment of the Dirac distribution in the kernel (7) of the collision term. In fact, this procedure enables us to transform the integral operator (6) with the nonregular kernel S into an integral-difference operator.

We consider the new unknown function Φ related to the electron distribution function via

$$\Phi(t, x, y, w, \mu, \varphi) = s(w) f(\mathrm{t}, \mathbf{x}, \mathbf{k}) \,,$$

where

$$s(w) = \sqrt{w(1 + \alpha_K w)}(1 + 2\alpha_K w). \tag{8}$$

Straightforward but cumbersome calculations end in the following transport equation for Φ:

$$\frac{\partial \Phi}{\partial t} + \frac{\partial}{\partial x}(g_1 \Phi) + \frac{\partial}{\partial y}(g_2 \Phi) + \frac{\partial}{\partial w}(g_3 \Phi) + \frac{\partial}{\partial \mu}(g_4 \Phi) + \frac{\partial}{\partial \varphi}(g_5 \Phi) = C(\Phi) \,. \tag{9}$$

The functions g_i $(i = 1, 2, .., 5)$ in the advection terms depend on the independent variables w, μ, φ as well as on time and position via the electric field. They are given by

$$
\begin{aligned}
g_1(\cdot) &= c_x \frac{\mu\sqrt{w(1+\alpha_K w)}}{1+2\alpha_K w}\,, \\
g_2(\cdot) &= c_x \frac{\sqrt{1-\mu^2}\sqrt{w(1+\alpha_K w)}\cos\varphi}{1+2\alpha_K w}\,, \\
g_3(\cdot) &= -2c_k \frac{\sqrt{w(1+\alpha_K w)}}{1+2\alpha_K w}\left[\mu\, E_x(t,x,y) + \sqrt{1-\mu^2}\cos\varphi\, E_y(t,x,\right. \\
g_4(\cdot) &= -c_k \frac{\sqrt{1-\mu^2}}{\sqrt{w(1+\alpha_K w)}}\left[\sqrt{1-\mu^2}\, E_x(t,x,y) - \mu\cos\varphi\, E_y(t,x,y\right. \\
g_5(\cdot) &= c_k \frac{\sin\varphi}{\sqrt{w(1+\alpha_K w)}\sqrt{1-\mu^2}}\, E_y(t,x,y)
\end{aligned}
$$

The right hand side of (9) is the integral-difference operator

$$C(\Phi)(t,x,y,w,\mu,\varphi) = s(w)\left\{c_0\int_0^{\pi}d\varphi'\int_{-1}^{1}d\mu'\,\Phi(t,x,y,w,\mu',\varphi')\right.$$
$$+\int_0^{\pi}d\varphi'\int_{-1}^{1}d\mu'\,[c_+\Phi(t,x,y,w+\gamma,\mu',\varphi')$$
$$\left.+c_-\Phi(t,x,y,w-\gamma,\mu',\varphi')]\right\}$$
$$-2\pi[c_0 s(w)+c_+ s(w-\gamma)+c_- s(w+\gamma)]\Phi(t,x,y,w,\mu,\varphi)\,,$$

where

$$(c_0,c_+,c_-) = \frac{2m^*\,t_*}{\hbar^3}\sqrt{2\,m^*\,k_B T_L}\,(K_0,(n_q+1)K,n_q K)\,,\quad \gamma=\frac{\hbar\omega_p}{k_B T_L}$$

are dimensionless parameters.

We remark that the δ distributions in the kernel S have been eliminated which leads to the shifted arguments of Φ.

In terms of the new variables the electron density becomes

$$n(t_* t, \ell_* x, \ell_* y) = \int_{\mathbb{R}^3} f(t_* t, \ell_* x, \ell_* y, \mathbf{k}) d\mathbf{k} = \left(\frac{\sqrt{2\, m^* k_B T_L}}{\hbar} \right)^3 \rho(t, x, y)\,,$$

where

$$\rho(t, x, y) = \int_0^{+\infty} dw \int_{-1}^{1} d\mu \int_0^{\pi} d\varphi\, \Phi(t, x, y, w, \mu, \varphi)\,. \qquad (10)$$

Hence, the dimensionless Poisson equation writes

$$\frac{\partial}{\partial x}\left(\epsilon_r \frac{\partial \Psi}{\partial x} \right) + \frac{\partial}{\partial y}\left(\epsilon_r \frac{\partial \Psi}{\partial y} \right) = c_p \left[\rho(t, x, y) - \mathcal{N}_D(x, y) \right] \qquad (11)$$

DG-BTE solver for 1D diodes simulation

The Boltzmann-Poisson system is solved on the domain

$$x \in [0, L], \quad w \in [0, w_{\text{max}}], \quad \mu \in [-1, 1],$$

where L is the dimensionless length of the device and w_{max} is the maximum value of the energy, which is adjusted in the numerical experiments such that

$$\Phi(t, x, w, \mu) \approx 0 \qquad \text{for } w \geq w_{\text{max}} \quad \text{and every} \quad t, x, \mu.$$

The initial value of f is a locally Maxwellian distribution at the temperature T_L,

$$\Phi(0, x, w, \mu) = s(w) N_D(x) e^{-w} \mathcal{M}$$

with the numerical parameter $\mathcal{M}$ chosen so that the initial value for the density is equal to the doping $N_D(x)$.

We use rectangular (but possibly non-uniform) meshes and P^1 elements, upwind numerical fluxes, and second-order Runge-Kutta time discretization. The code is written in an efficient matrix-vector multiplication format with precomputed and stored matrices to save computational costs.

The Poisson equation is solved by an LDG method.

We consider two test examples: Si $n^+ - n - n^+$ diodes of a total length of 1 and $0.25\mu m$, with 400 and $50nm$ channels located in the middle of the device, respectively. For the $400nm$ channel device, the dimensional doping is given by $N_D = 5 \times 10^{17} cm^{-3}$ in the n^+ region and $N_D = 2 \times 10^{15} cm^{-3}$ in the n^- region. For the $50nm$channel device, the dimensional doping is given by $N_D = 5 \times 10^{18} cm^{-3}$ in the n^+ region and $N_D = 1 \times 10^{15} cm^{-3}$ in the n^- region. Both examples were computed by WENO before.

The nonuniform mesh we use for $400nm$ channels is defined as follows. In the x-direction, if $x < 0.2$ or $x > 0.4$, $\triangle x = 0.01$. In the region $0.2 < x < 0.4$, $\triangle x = 0.005$. Thus, the total number of cells in x direction is 120. In the w-direction, we use 60 uniform cells. In the μ-direction, we use 24 cells, 12 in the region $\mu < 0.7$, 12 in $\mu > 0.7$. Thus, the grid consists of $120 \times 60 \times 24$ cells, compared to the WENO grid of $180 \times 60 \times 24$ uniform cells.

We plot the evolution of density, mean velocity, energy and momentum in the next two figures. The solution has already stabilized at $t = 5.0$ from the momentum plots.

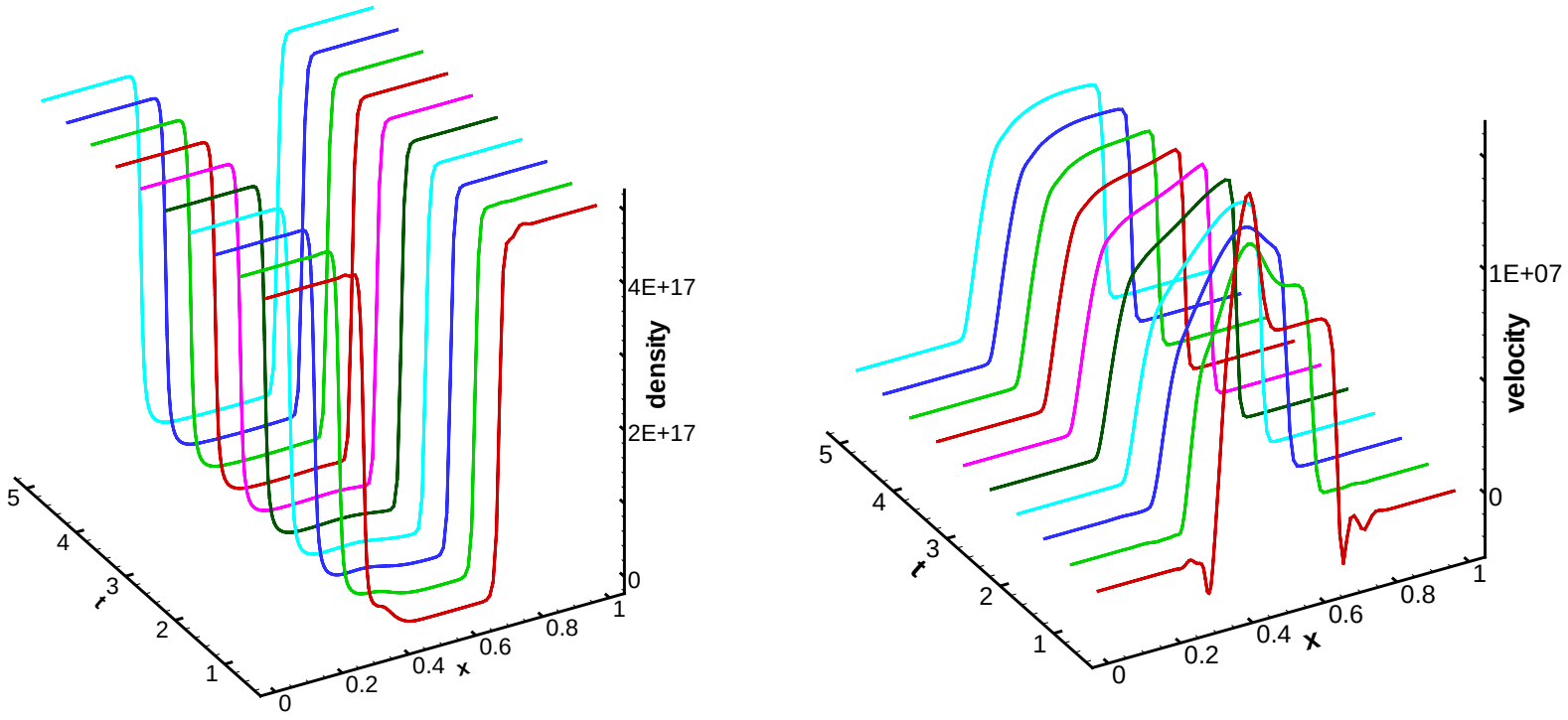

Figure 3: Time evolution of macroscopic quantities using DG method for 400nm channel at $V_{\text{bias}} = 1.0$. Left: density in cm^{-3}; right: mean velocity in cm/s.

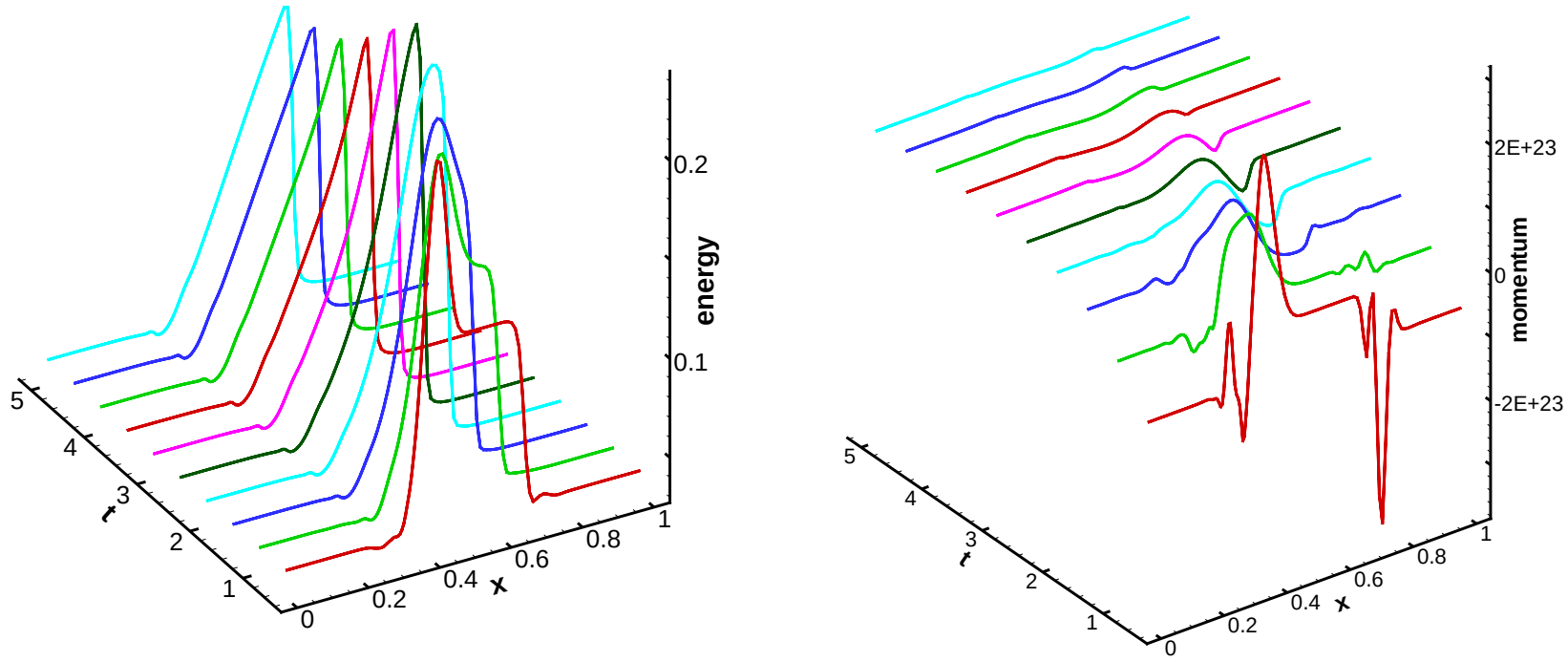

Figure 4: Time evolution of macroscopic quantities using DG method for 400nm channel at $V_{\text{bias}} = 1.0$. Left: energy in eV; right: momentum in $cm^{-2}\, s^{-1}$.

The macroscopic quantities at steady state are plotted in the next figures. The results are compared with the WENO calculation. They agree with each other in general, with DG offering more resolution and a higher peak in energy near the junctions.

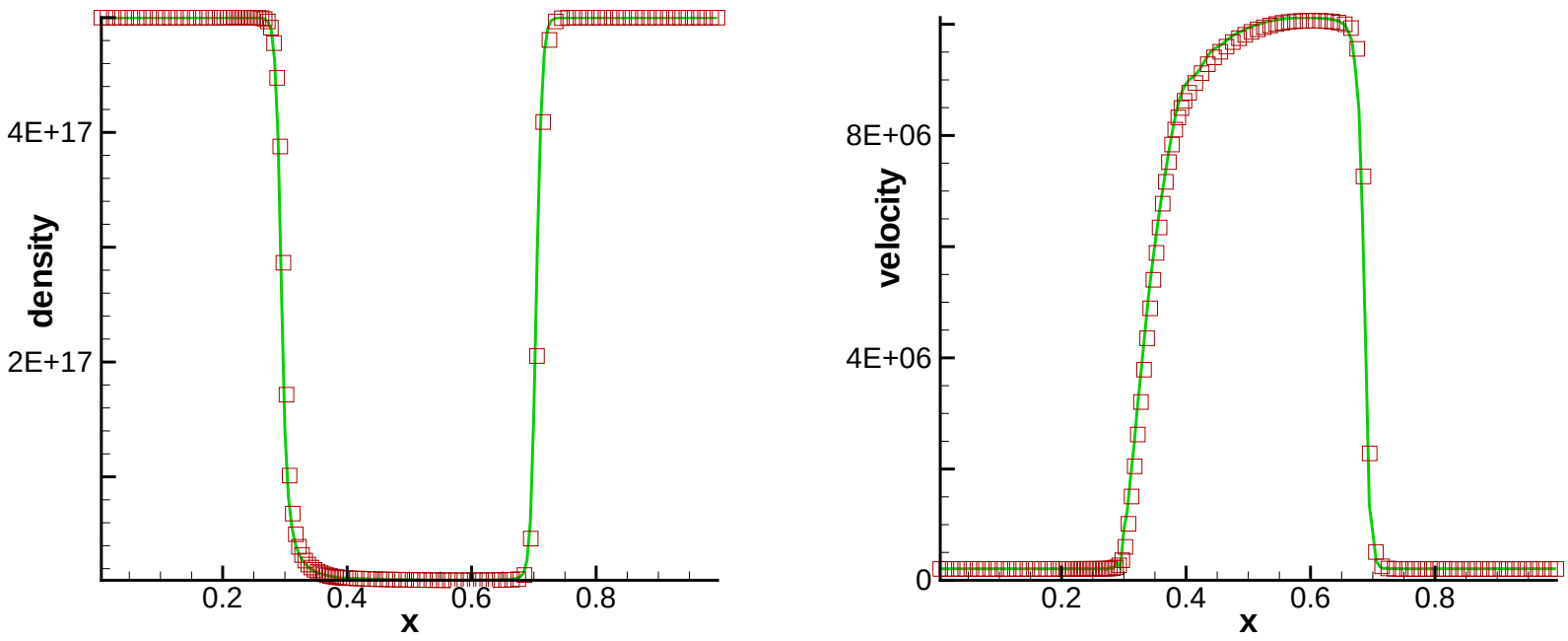

Figure 5: Comparison of macroscopic quantities using DG (symbols) and WENO (solid line) for 400nm channel at $t = 5.0$, $V_{\text{bias}} = 1.0$. Left: density in cm^{-3}; right: mean velocity in cm/s. Solution has reached steady state.

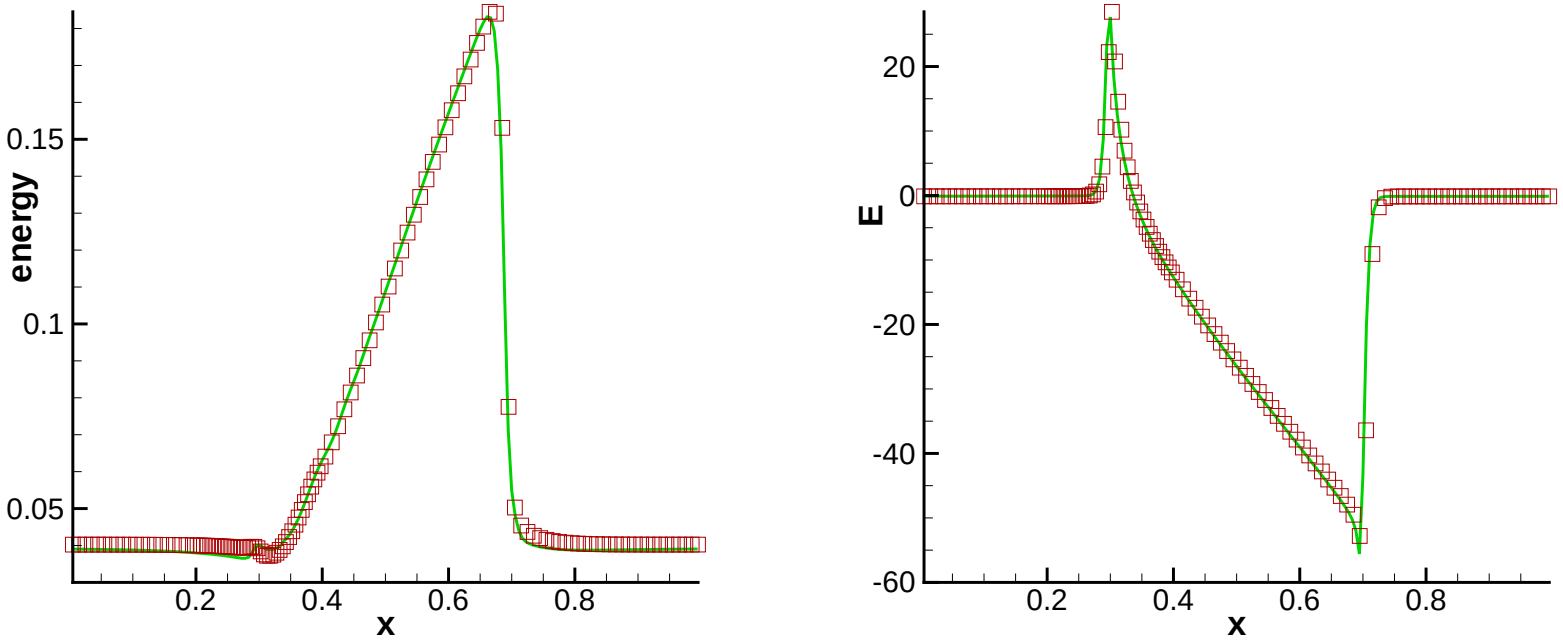

Figure 6: Comparison of macroscopic quantities using DG (symbols) and WENO (solid line) for 400nm channel at $t = 5.0$, $V_{\text{bias}} = 1.0$. Left: energy in eV; right: electric field in kV/cm. Solution has reached steady state.

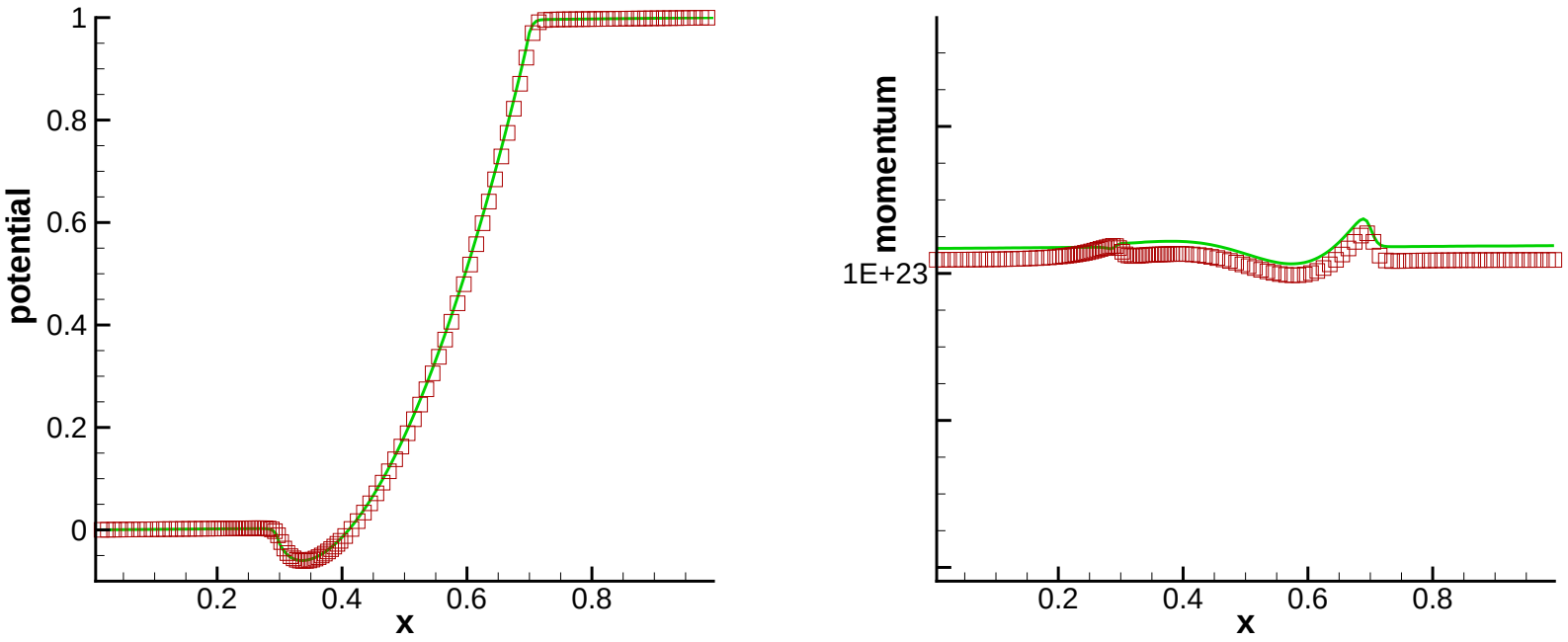

Figure 7: Comparison of macroscopic quantities using DG (symbols) and WENO (solid line) for 400nm channel at $t = 5.0$, $V_{\text{bias}} = 1.0$. Left: potential in V; right: momentum in $cm^{-2}\, s^{-1}$. Solution has reached steady state.

The next figures show comparisons for the *pdf* at transient and steady state. We plot at different position of the device, namely, the left, center and right of the channel. We notice a larger value of *pdf* especially at the center of the channel, where the *pdf* is no longer Maxwellian. Moreover, at $t = 0.5$, $x_0 = 0.5$, the *pdf* shows a double hump structure, which is not captured by the WENO solver. All of these advantages come from the fact that we are refining more near $\mu = 1$.

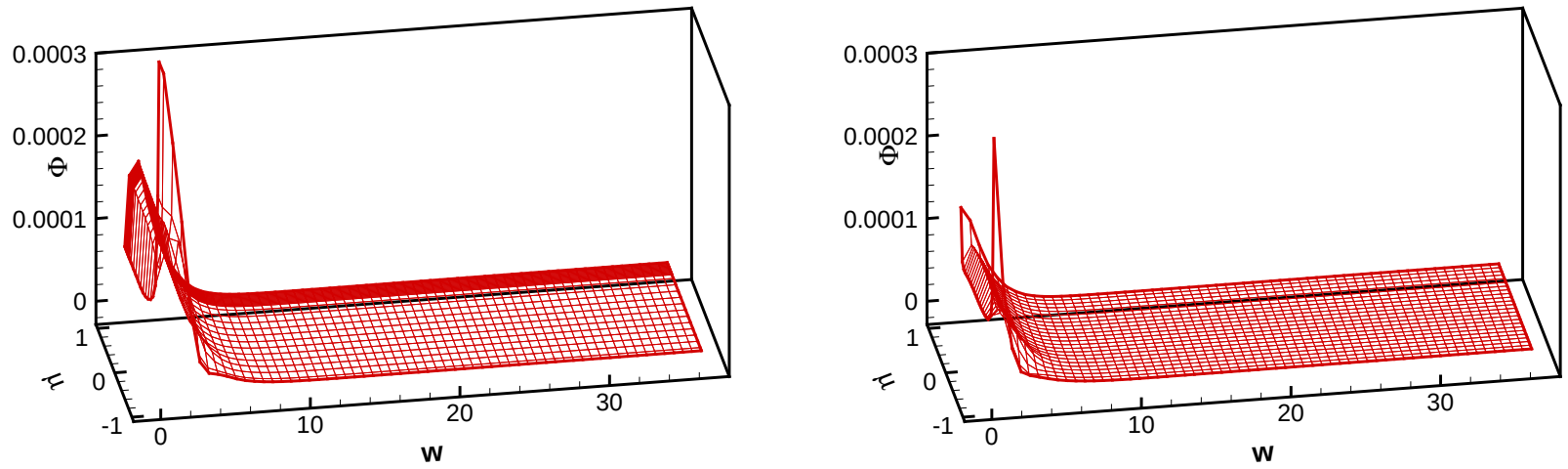

Figure 8: Comparison of the snapshot for $\Phi(x_0, w, \mu)$ using DG (left) and WENO (right) for 400nm channel at $t = 0.5$, $V_{\text{bias}} = 1.0$. $x_0 = 0.3$. Solution has not yet reached steady state.

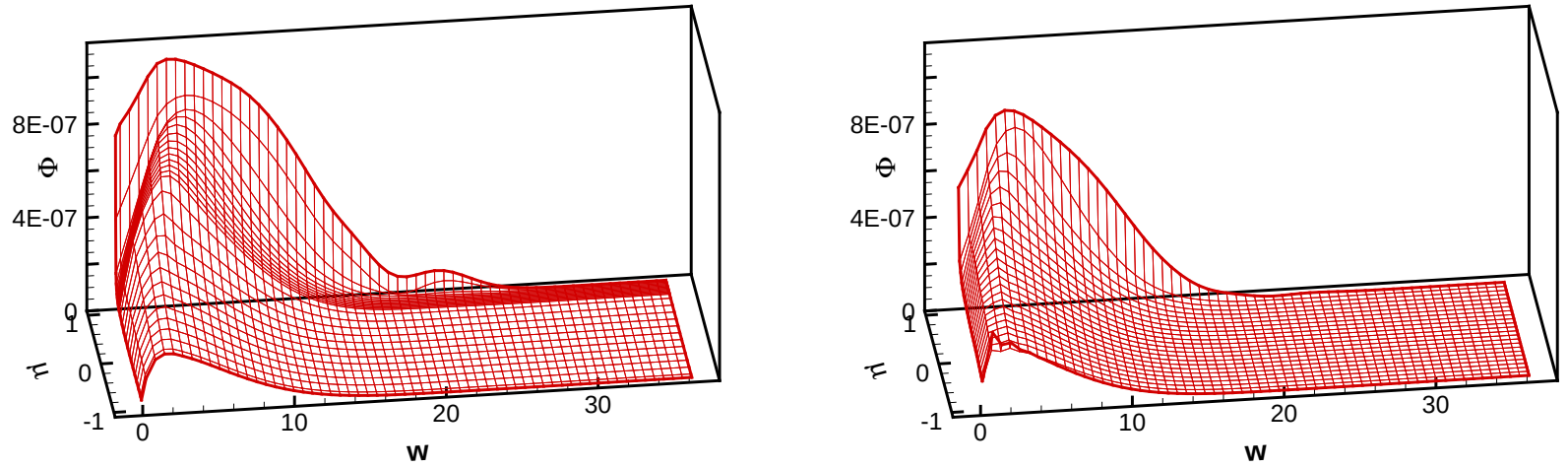

Figure 9: Comparison of the snapshot for $\Phi(x_0, w, \mu)$ using DG (left) and WENO (right) for 400nm channel at $t = 0.5$, $V_{\text{bias}} = 1.0$. $x_0 = 0.5$. Solution has not yet reached steady state.

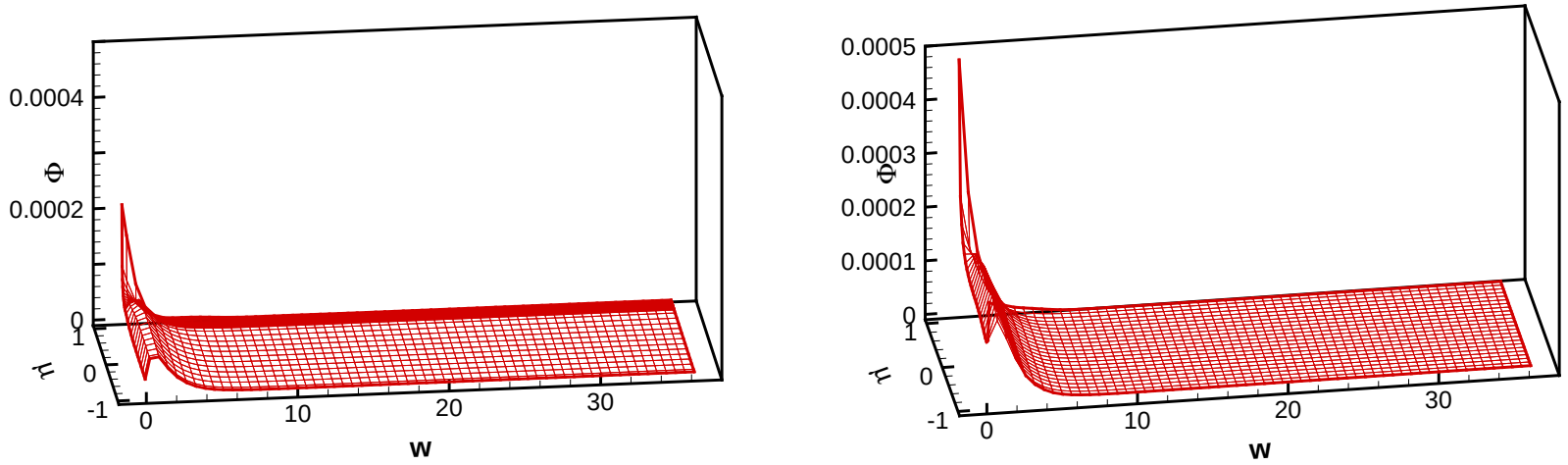

Figure 10: Comparison of the snapshot for $\Phi(x_0, w, \mu)$ using DG (left) and WENO (right) for 400nm channel at $t = 0.5$, $V_{\text{bias}} = 1.0$. $x_0 = 0.7$. Solution has not yet reached steady state.

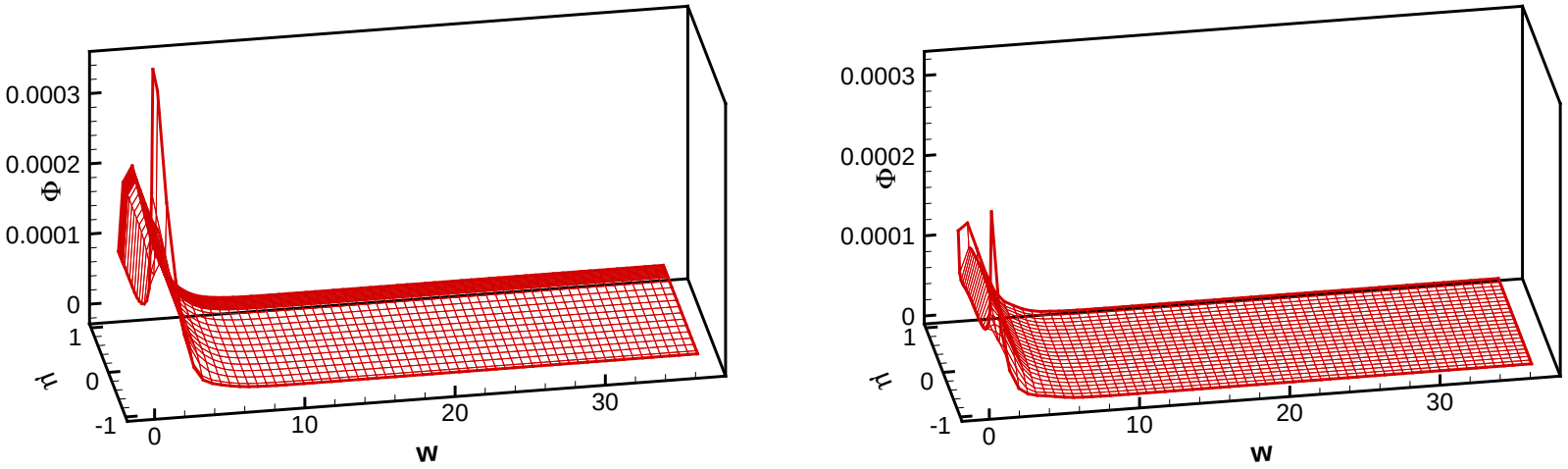

Figure 11: Comparison of the snapshot for $\Phi(x_0, w, \mu)$ using DG (left) and WENO (right) for 400nm channel at $t = 5.0$, $V_{\text{bias}} = 1.0$. $x_0 = 0.3$. Solution has reached steady state.

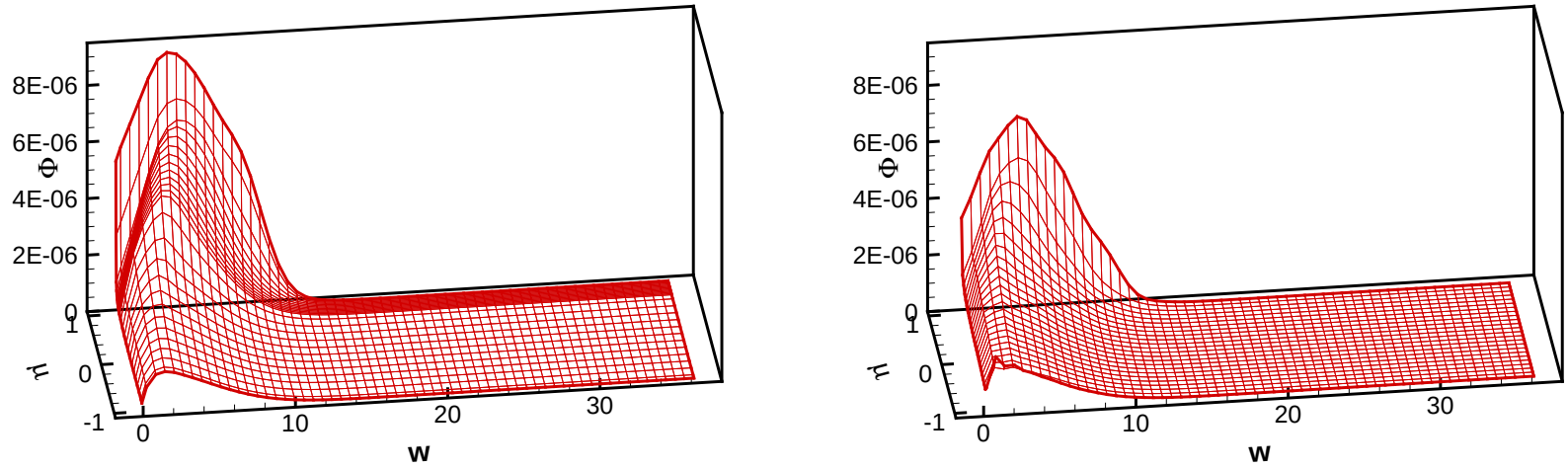

Figure 12: Comparison of the snapshot for $\Phi(x_0, w, \mu)$ using DG (left) and WENO (right) for 400nm channel at $t = 5.0$, $V_{\text{bias}} = 1.0$. $x_0 = 0.5$. Solution has reached steady state.

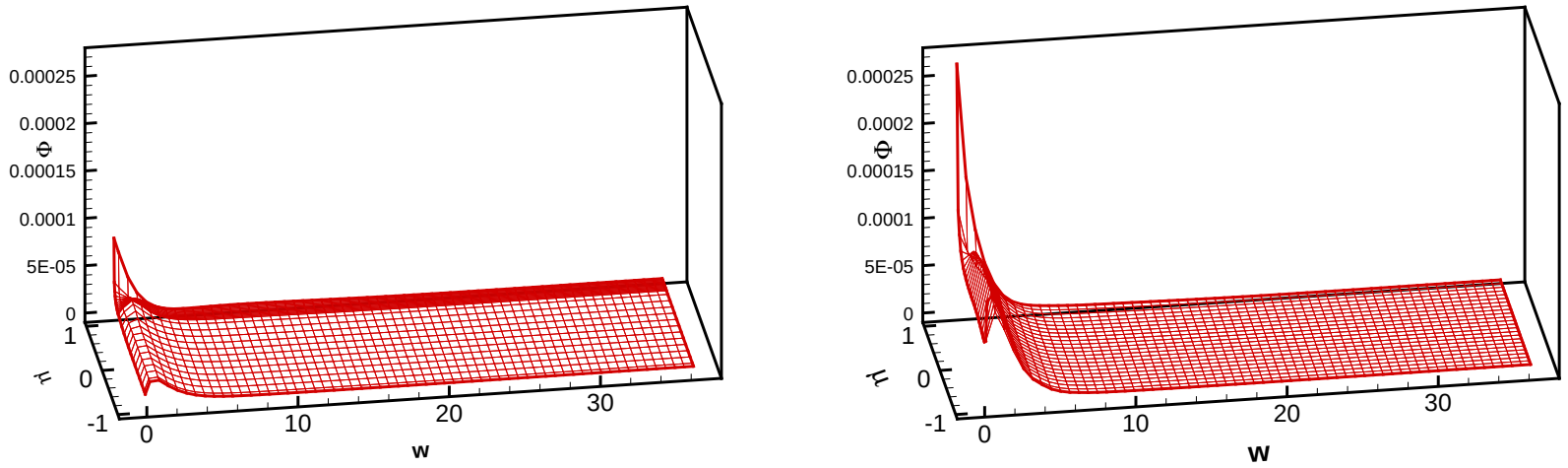

Figure 13: Comparison of the snapshot for $\Phi(x_0, w, \mu)$ using DG (left) and WENO (right) for 400nm channel at $t = 5.0$, $V_{\text{bias}} = 1.0$. $x_0 = 0.7$. Solution has reached steady state.

To have a better idea of the shape of the *pdf*, we plot $\Phi(t = 5.0, x = 0.5)$ in the cartesian coordinates in the next figure. The coordinate $V1$ in the plot is the momentum parallel to the force field k_1, $V2$ is the modulus of the orthogonal component. The peak is captured very sharply compared to WENO.

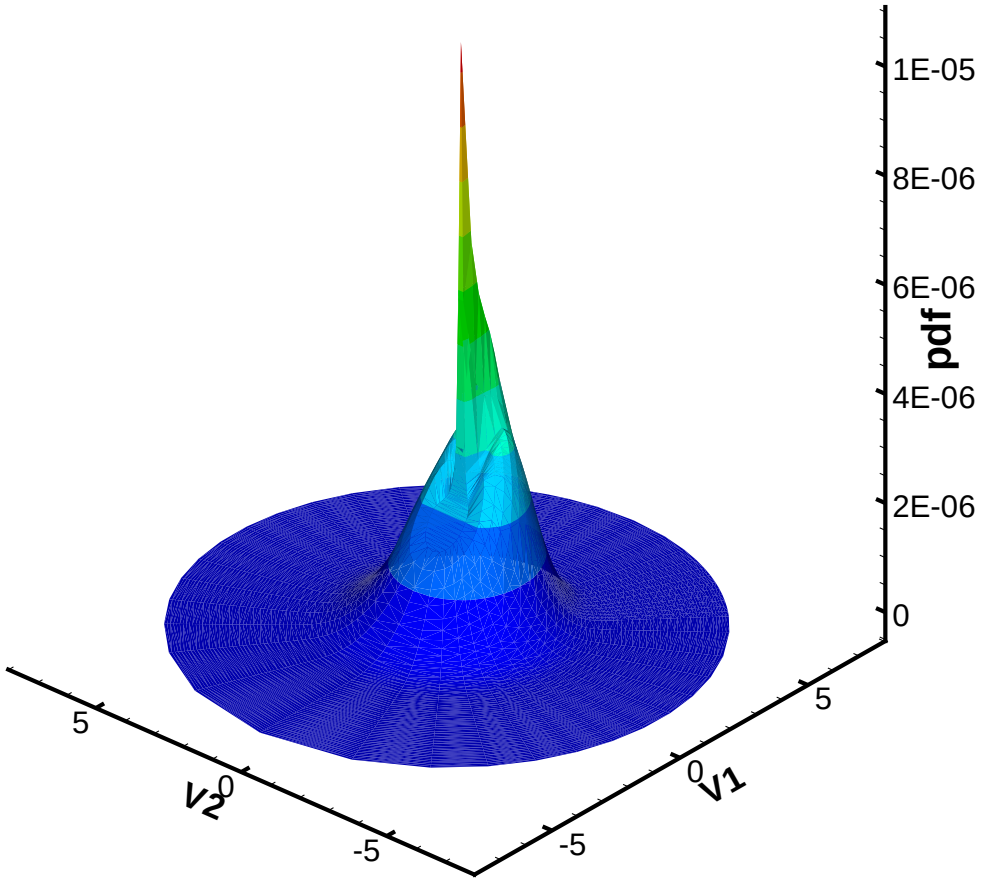

Figure 14: PDF for 400nm channel at $t = 5.0$, $x = 0.5$.

The nonuniform mesh we use for $50nm$ channels is defined as follows. In the x-direction, near the junctions, in $0.09 < x < 0.11$ and $0.14 < x < 0.16$, $\triangle x = 0.001$; in center of the channel $0.11 < x < 0.14$, $\triangle x = 0.005$; at everywhere else, $\triangle x = 0.01$. Thus, the total number of cells in x direction is 64. In the w-direction, we use 60 uniform cells. In the μ-direction, we use 20 cells, 10 in the region $\mu < 0.7$, 10 in $\mu > 0.7$. Thus, the grid consists of $64 \times 60 \times 20$ cells, compared to the WENO calculation of $150 \times 120 \times 16$ uniform cells.

The evolution and steady state plots are listed in the following figures. The conclusions are similar with $400nm$, that we obtain better resolutions near the channel junctions and the peak for *pdf* is much higher.

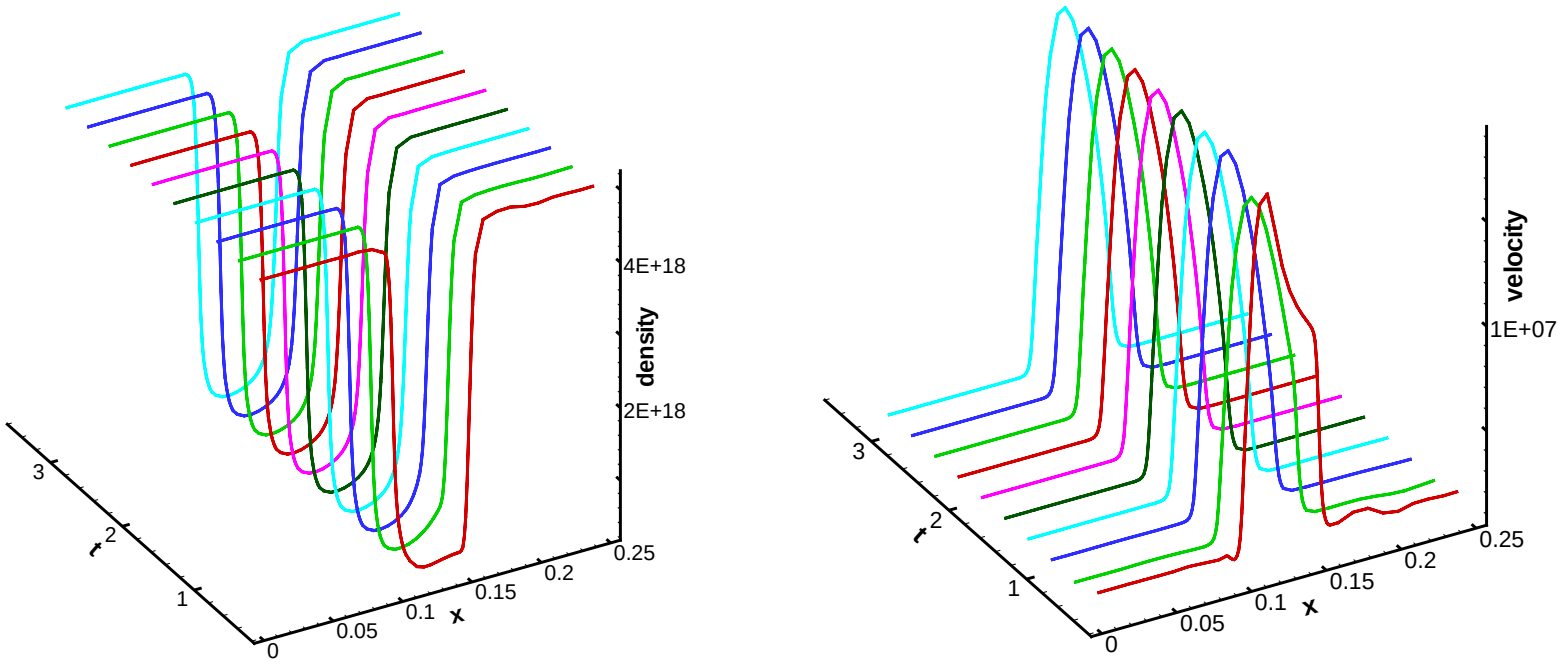

Figure 15: Time evolution of macroscopic quantities using DG method for 50nm channel at $V_{\text{bias}} = 1.0$. Left: density in cm^{-3}; right: mean velocity in cm/s.

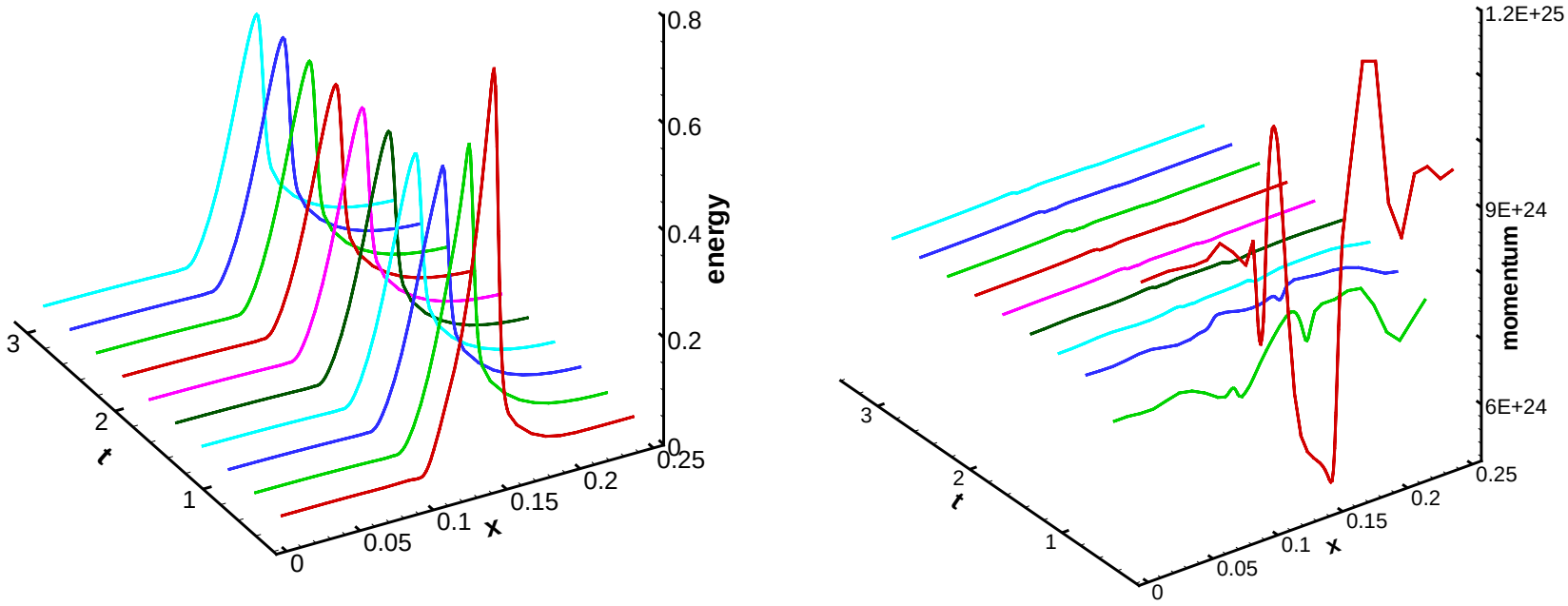

Figure 16: Time evolution of macroscopic quantities using DG method for 50nm channel at $V_{\text{bias}} = 1.0$. Left: energy in eV; right: momentum in $cm^{-2}\, s^{-1}$.

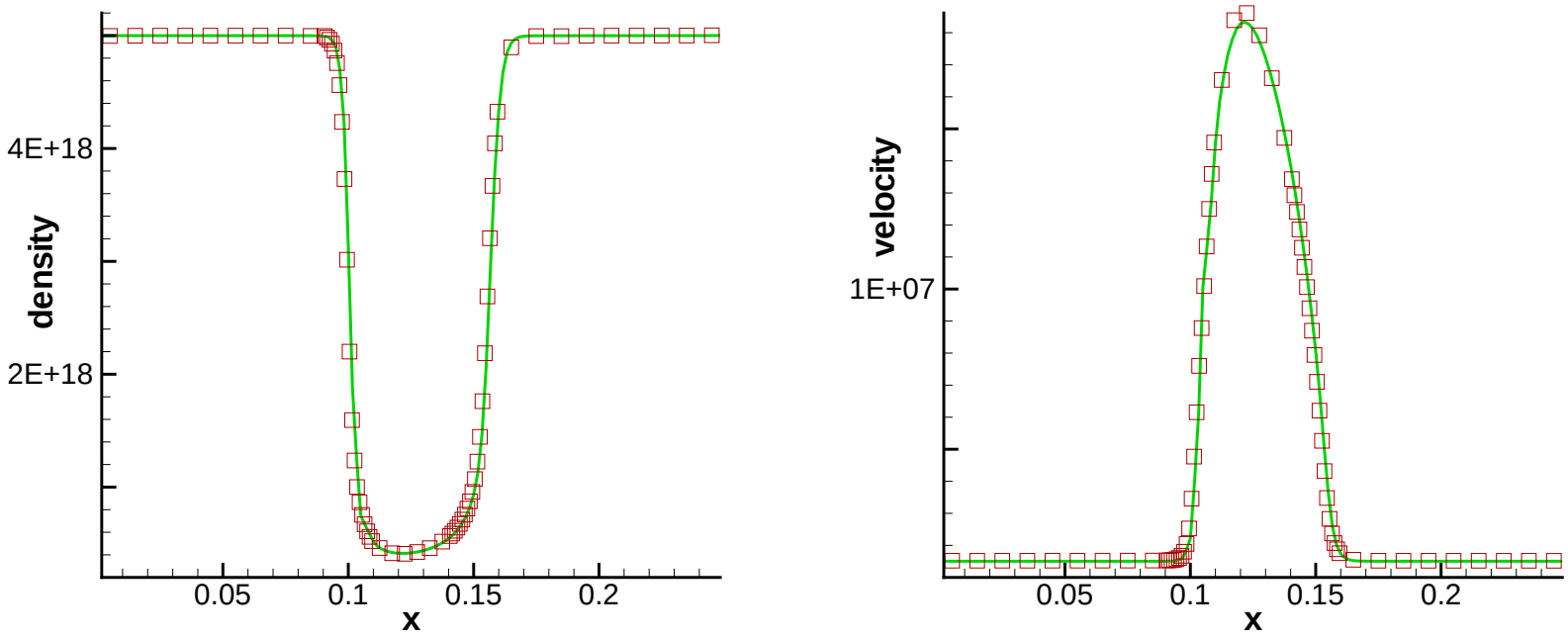

Figure 17: Comparison of macroscopic quantities using DG (symbols) and WENO (solid line) for 50nm channel at $t = 3.0$, $V_{\text{bias}} = 1.0$. Left: density in cm^{-3}; right: mean velocity in cm/s. Solution has reached steady state.

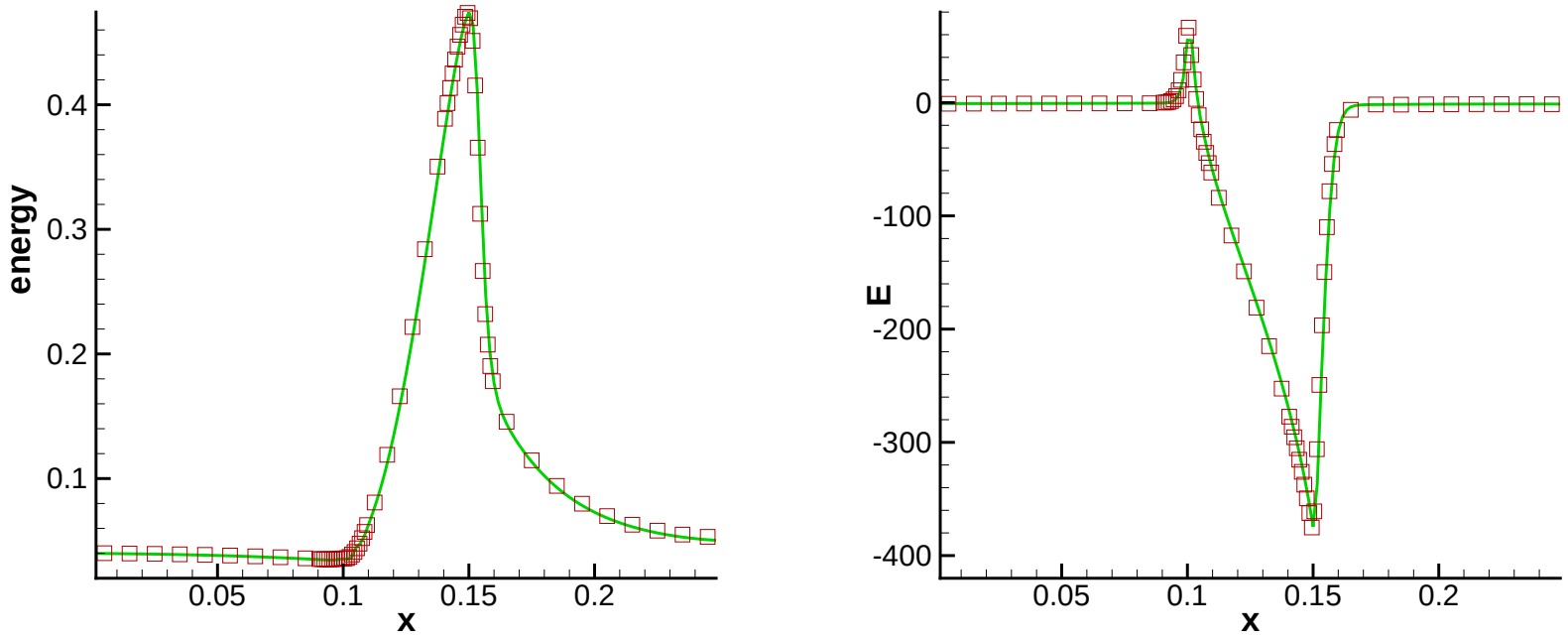

Figure 18: Comparison of macroscopic quantities using DG (symbols) and WENO (solid line) for 50nm channel at $t = 3.0$, $V_{\text{bias}} = 1.0$. Left: energy in eV; right: electric field in kV/cm. Solution has reached steady state.

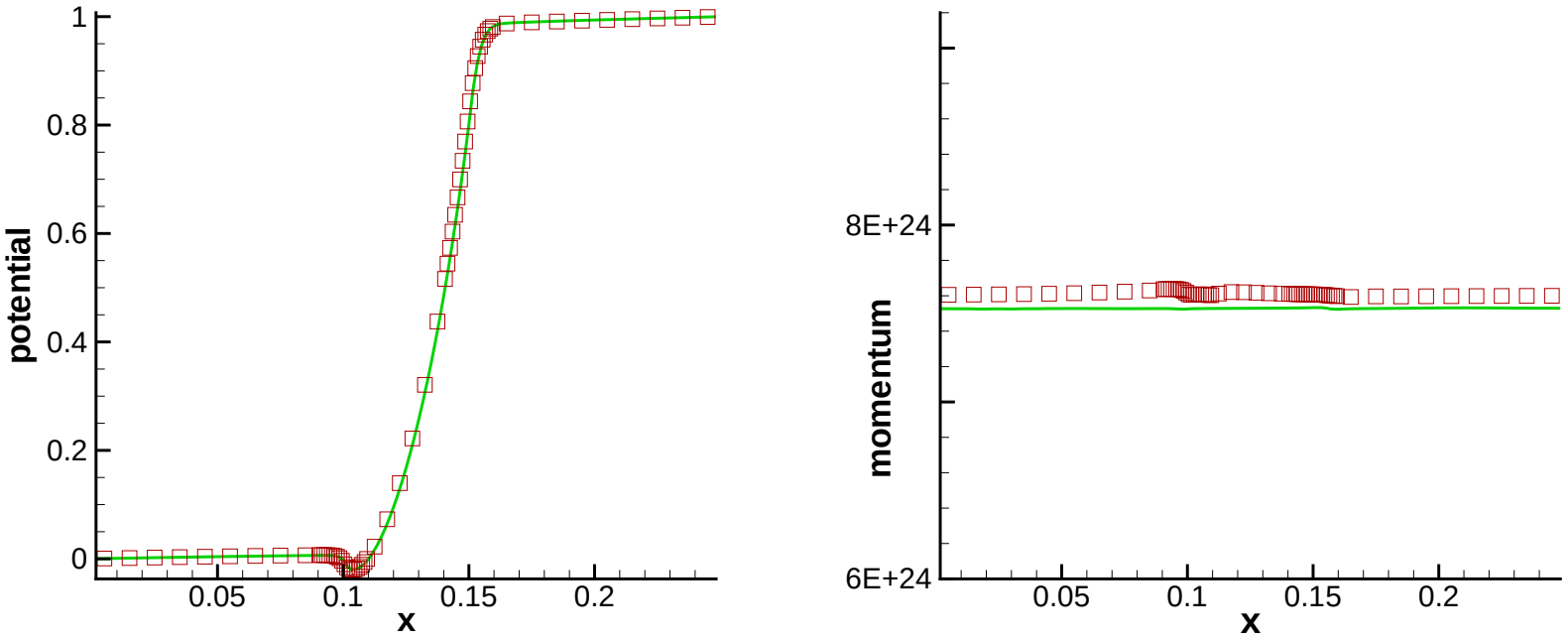

Figure 19: Comparison of macroscopic quantities using DG (symbols) and WENO (solid line) for 50nm channel at $t = 3.0$, $V_{\text{bias}} = 1.0$. Left: potential in V; right: momentum in $cm^{-2}\, s^{-1}$. Solution has reached steady state.

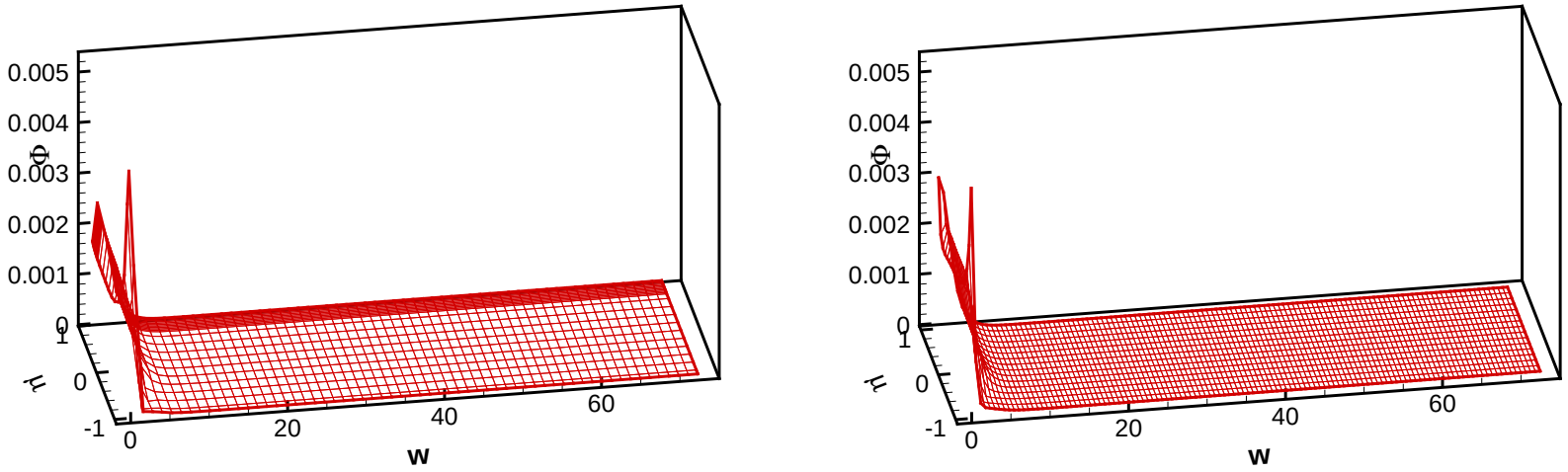

Figure 20: Comparison of the snapshot for $\Phi(x_0, w, \mu)$ using DG (left) and WENO (right) for 50nm channel at $t = 0.5$, $V_{\text{bias}} = 1.0$. $x_0 = 0.1$. Solution has not yet reached steady state.

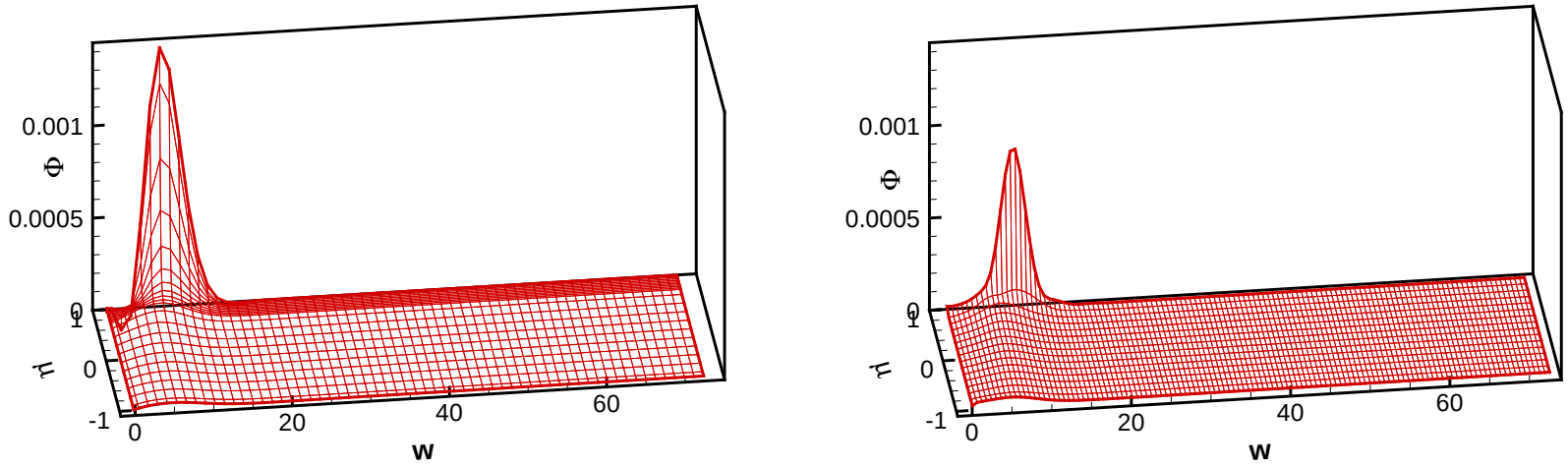

Figure 21: Comparison of the snapshot for $\Phi(x_0, w, \mu)$ using DG (left) and WENO (right) for 50nm channel at $t = 0.5$, $V_{\text{bias}} = 1.0$. $x_0 = 0.125$. Solution has not yet reached steady state.

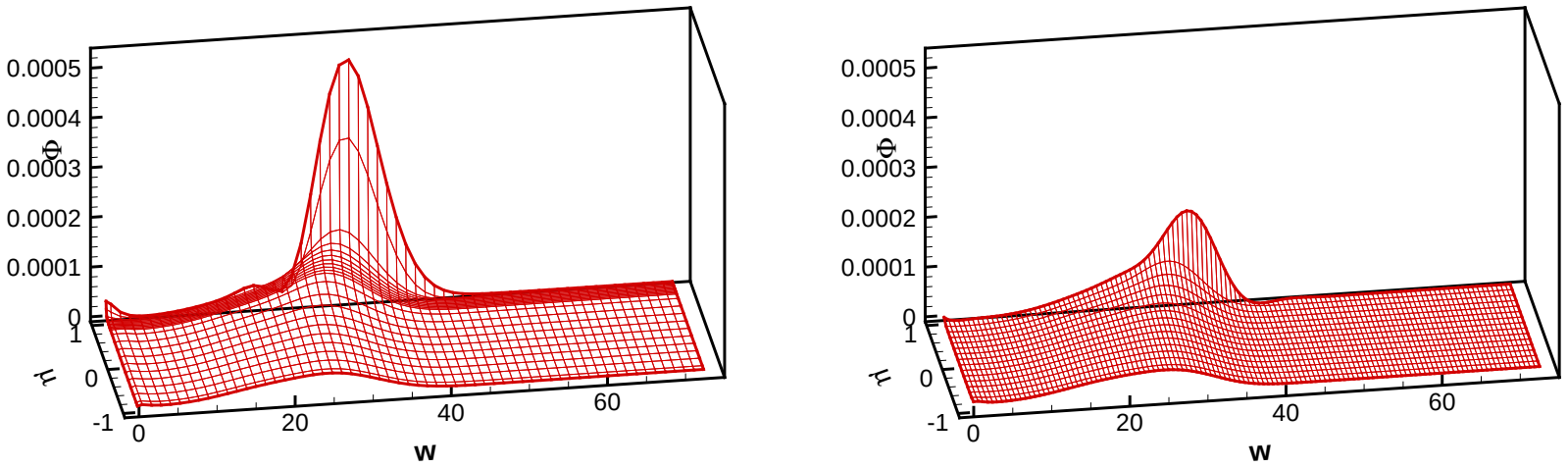

Figure 22: Comparison of the snapshot for $\Phi(x_0, w, \mu)$ using DG (left) and WENO (right) for 50nm channel at $t = 0.5$, $V_{\text{bias}} = 1.0$. $x_0 = 0.15$. Solution has not yet reached steady state.

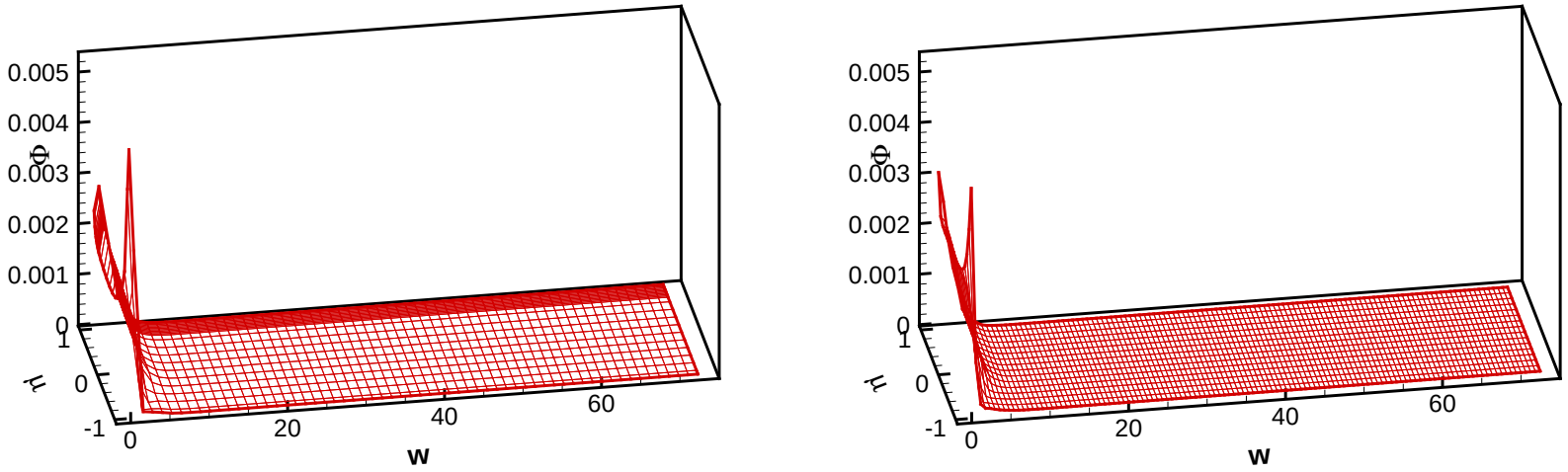

Figure 23: Comparison of the snapshot for $\Phi(x_0, w, \mu)$ using DG (left) and WENO (right) solution for 50nm channel at $t = 3.0$, $V_{\text{bias}} = 1.0$. $x_0 = 0.1$. Solution has reached steady state.

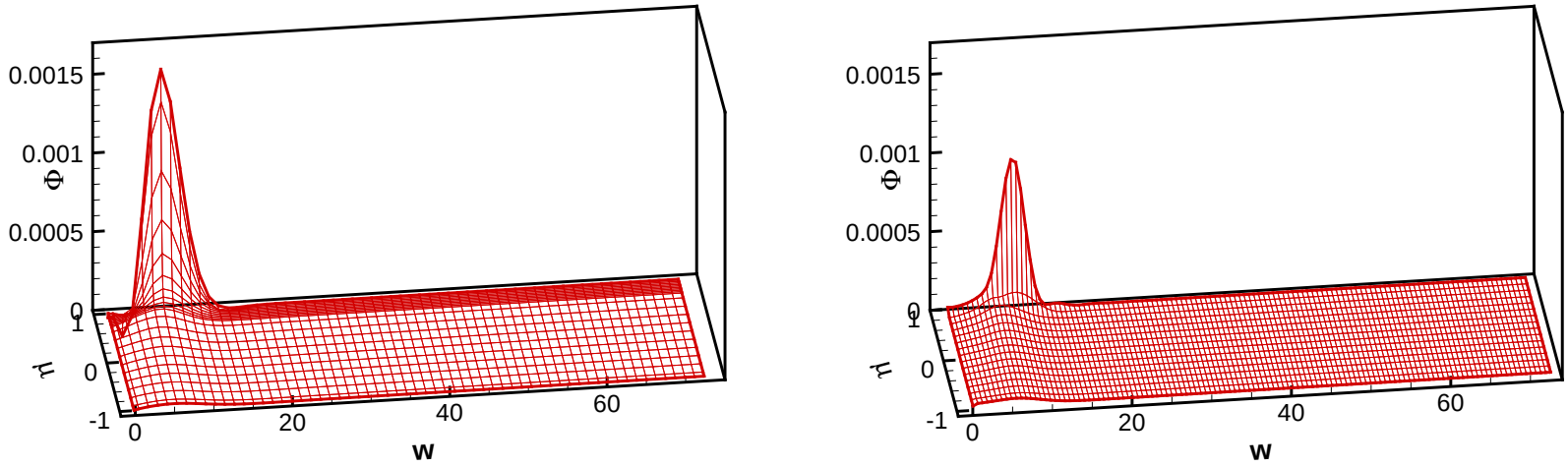

Figure 24: Comparison of the snapshot for $\Phi(x_0, w, \mu)$ using DG (left) and WENO (right) solution for 50nm channel at $t = 3.0$, $V_{\text{bias}} = 1.0$. $x_0 = 0.125$. Solution has reached steady state.

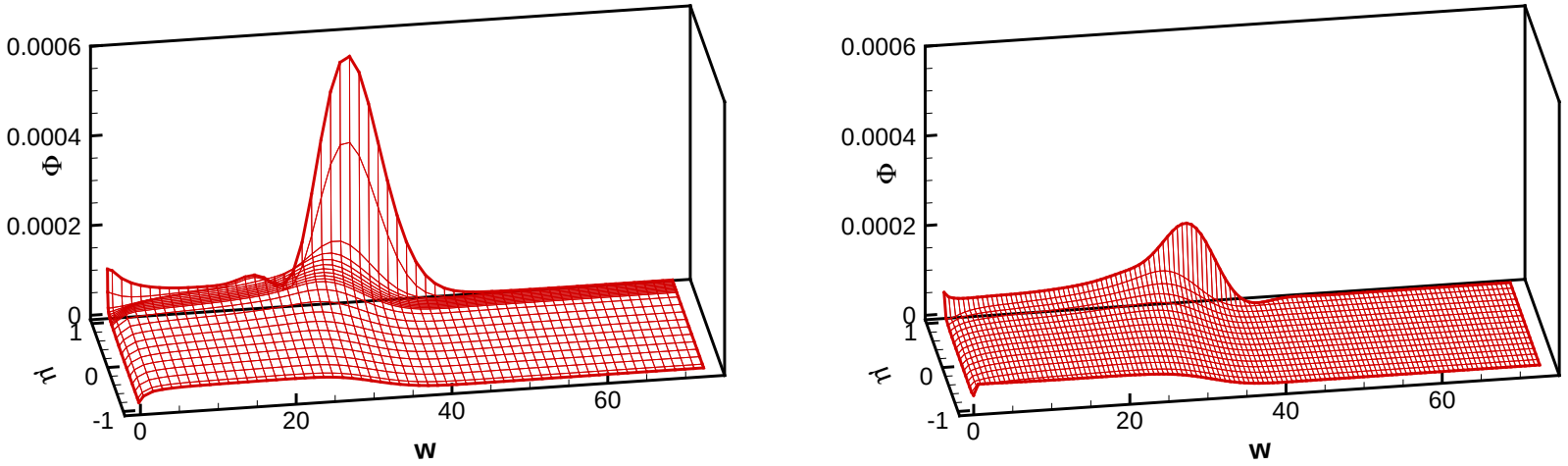

Figure 25: Comparison of the snapshot for $\Phi(x_0, w, \mu)$ using DG (left) and WENO (right) solution for 50nm channel at $t = 3.0$, $V_{\text{bias}} = 1.0$. $x_0 = 0.15$. Solution has reached steady state.

The next figure plots $\Phi(t = 5.0, x = 0.125)$ in the cartesian coordinates. The peak is twice the height of WENO and is very sharp. We also plot the *pdf* near $x = 0.15$, the drain junction. We obtain distributions far away from statistical equilibrium, that reflects the lack of suitability of the classical hydrodynamical models for the drain region of a small gated device under even moderate voltage bias.

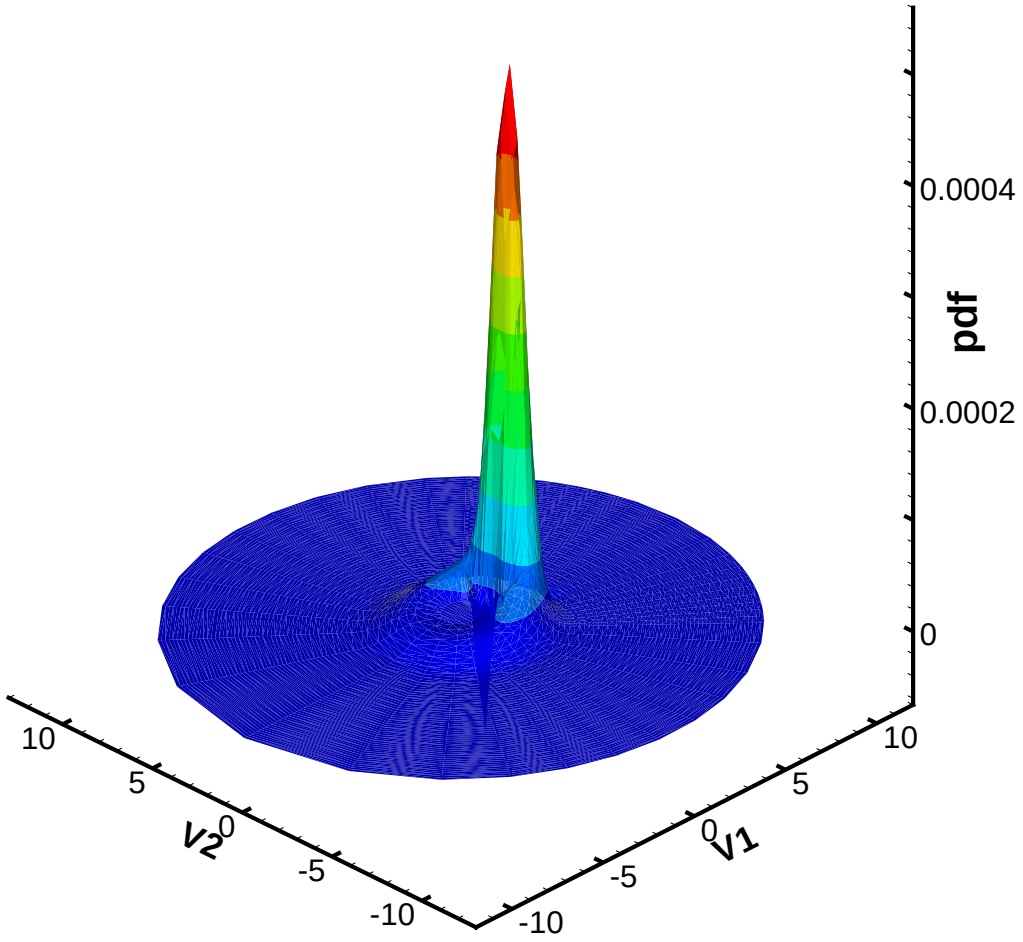

Figure 26: PDF for 50nm channel at $t = 3.0$, $x = 0.125$.

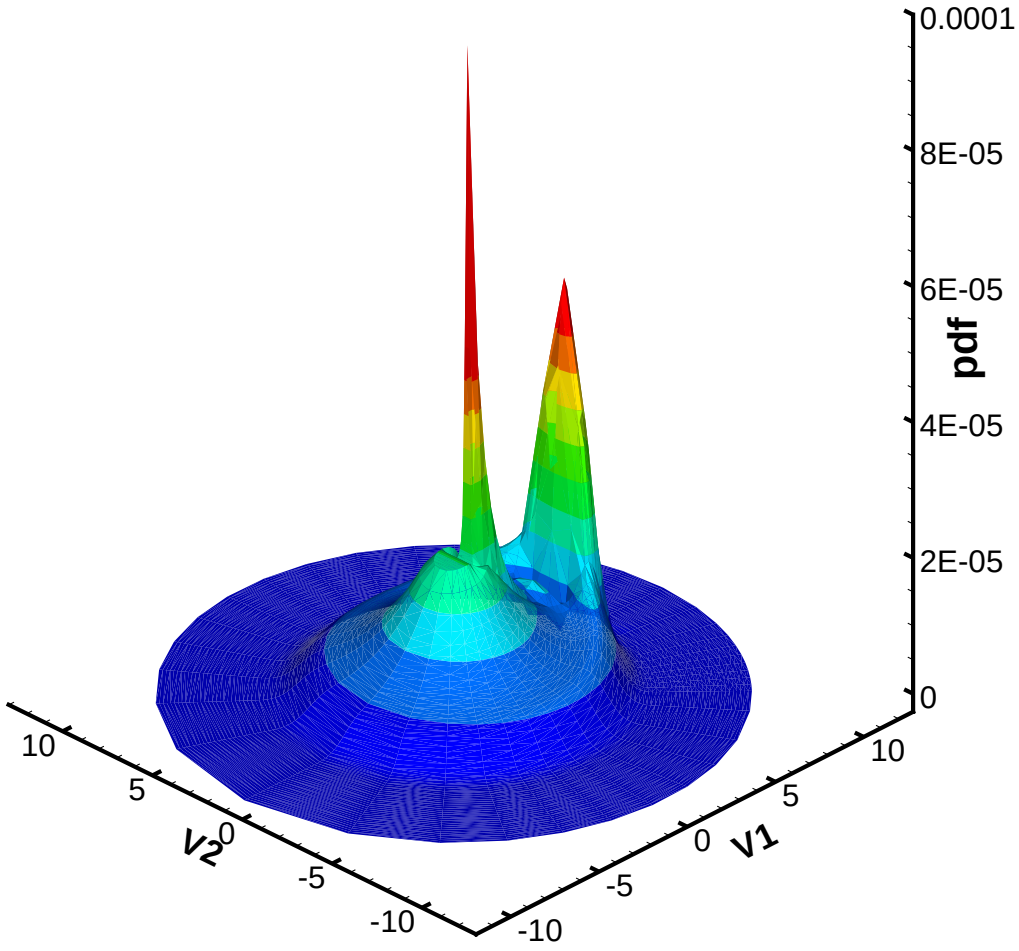

Figure 27: PDF for 50nm channel at $t = 3.0$, $x = 0.149$.

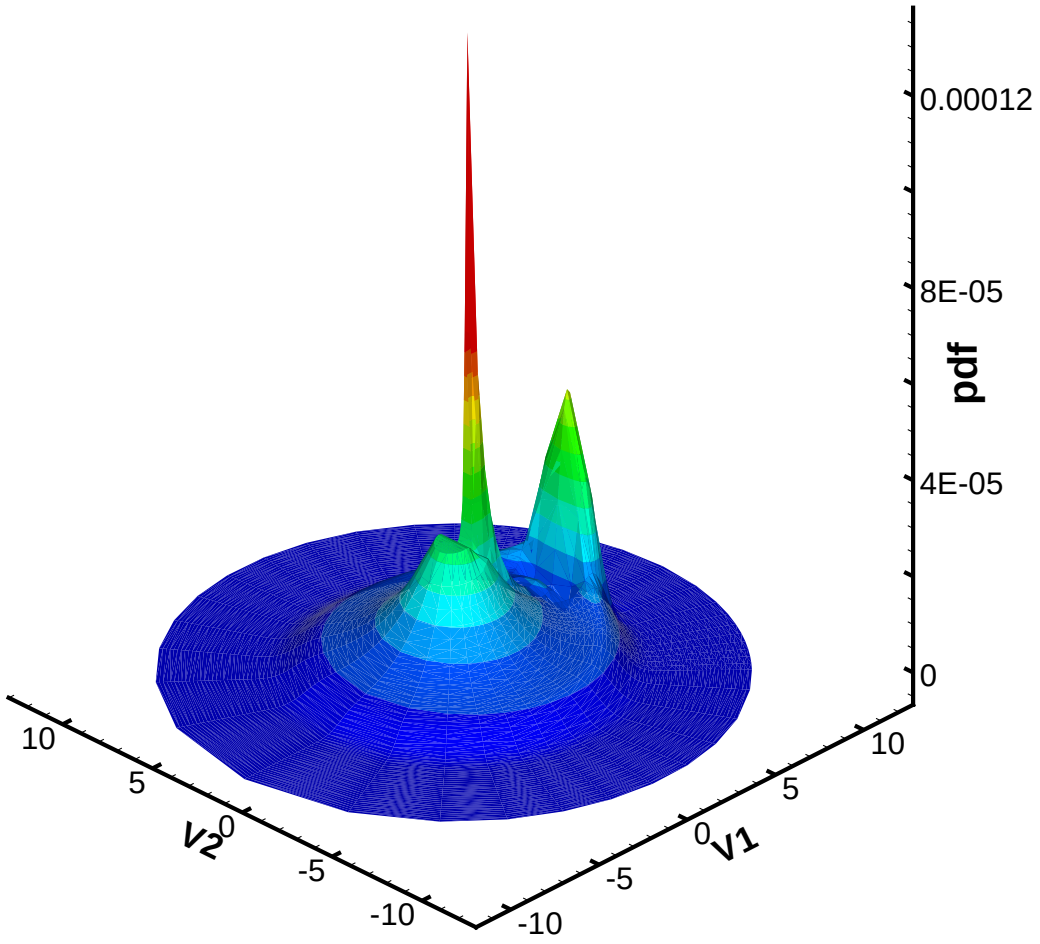

Figure 28: PDF for 50nm channel at $t = 3.0$, $x = 0.15$.

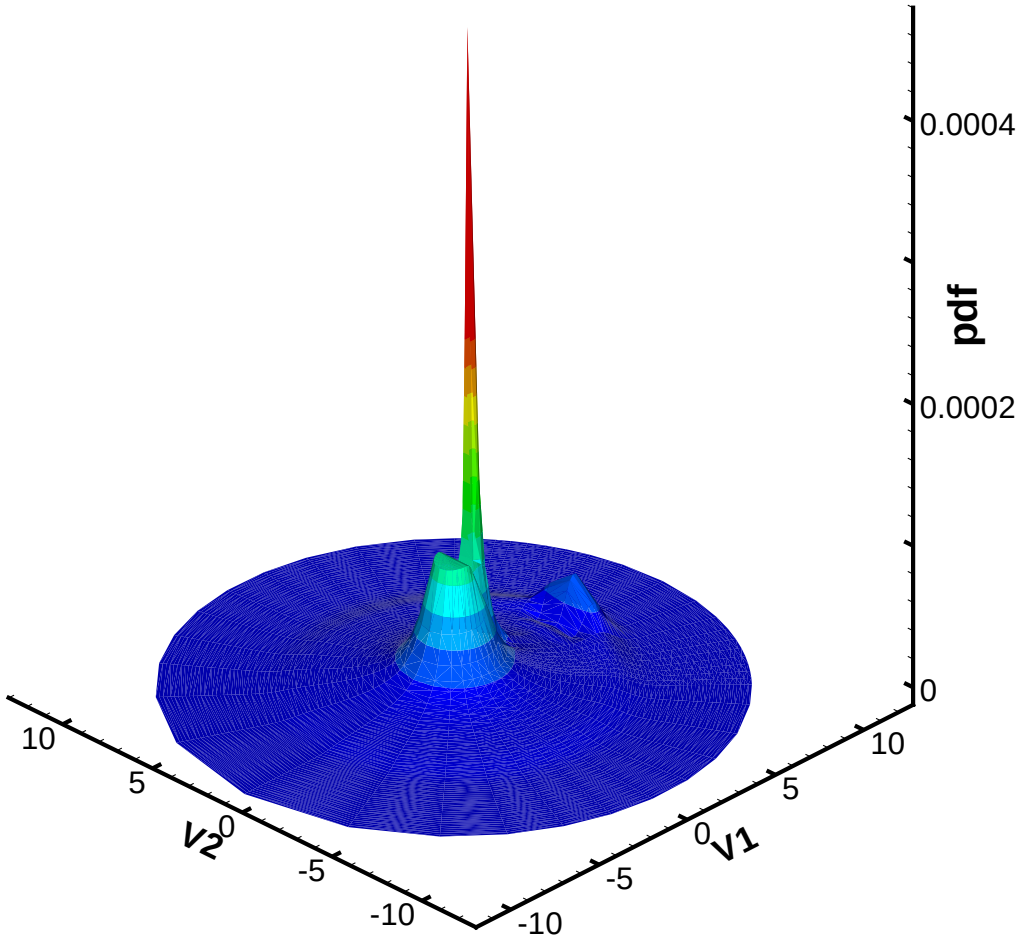

Figure 29: PDF for 50nm channel at $t = 3.0$, $x = 0.152$.

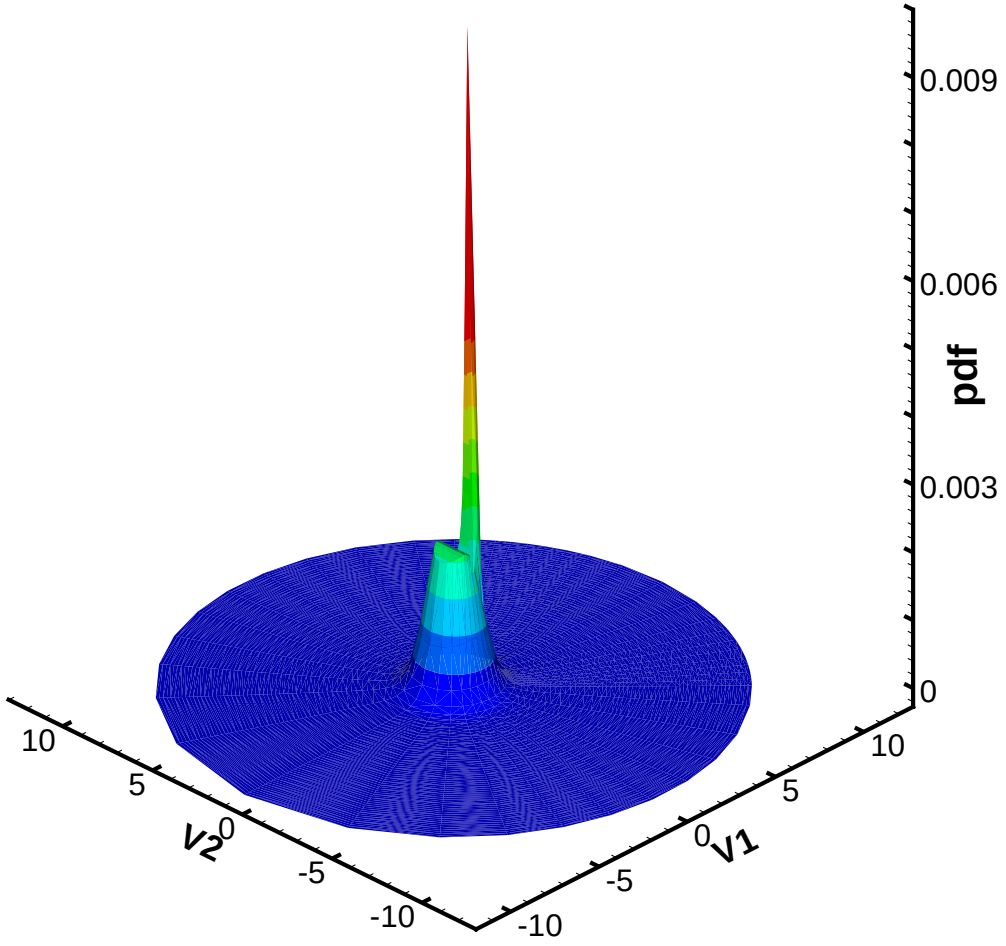

Figure 30: PDF for 50nm channel at $t = 3.0$, $x = 0.16$.

We also compare the results from DG-BTE solver with those obtained from DSMC simulations. The two simulations show good agreement except for energy plots near the boundaries. Now, it is obvious that the difference in the boundary treatment has an influence for the solutions at the stationary regime.

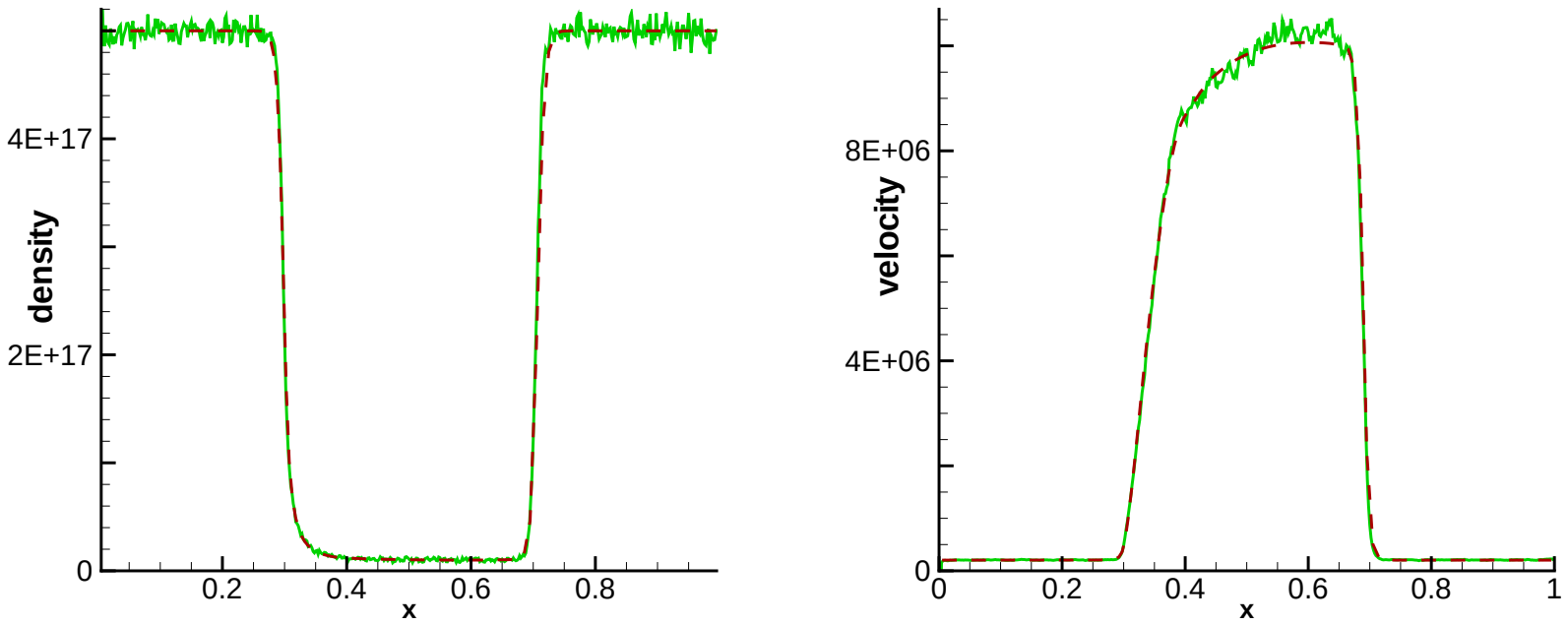

Figure 31: Comparison of macroscopic quantities using DG (dashed line) and DSMC (solid line) for 400nm channel at $t = 5.0$, $V_{\text{bias}} = 1.0$. Left: density in cm^{-3}; right: mean velocity in cm/s. Solution has reached steady state.

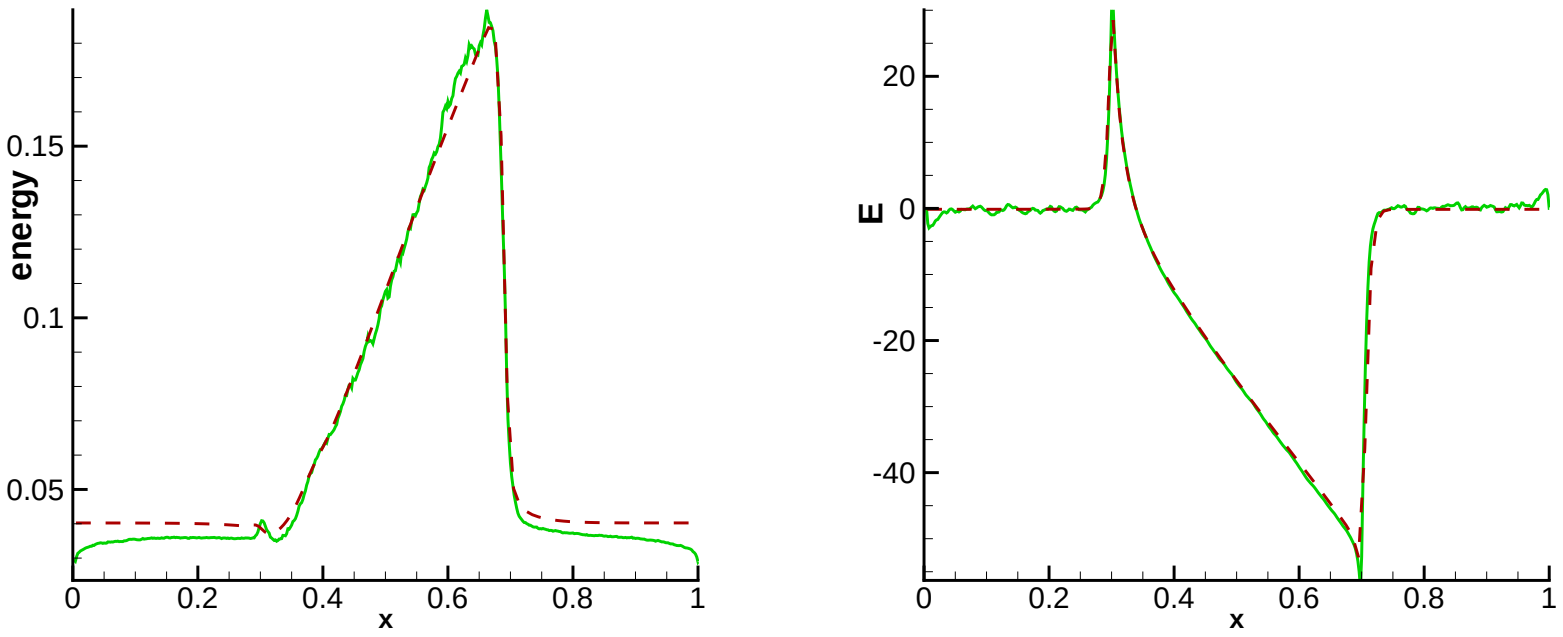

Figure 32: Comparison of macroscopic quantities using DG (dashed line) and DSMC (solid line) for 400nm channel at $t = 5.0$, $V_{\text{bias}} = 1.0$. Left: energy in eV; right: electric field in kV/cm. Solution has reached steady state.

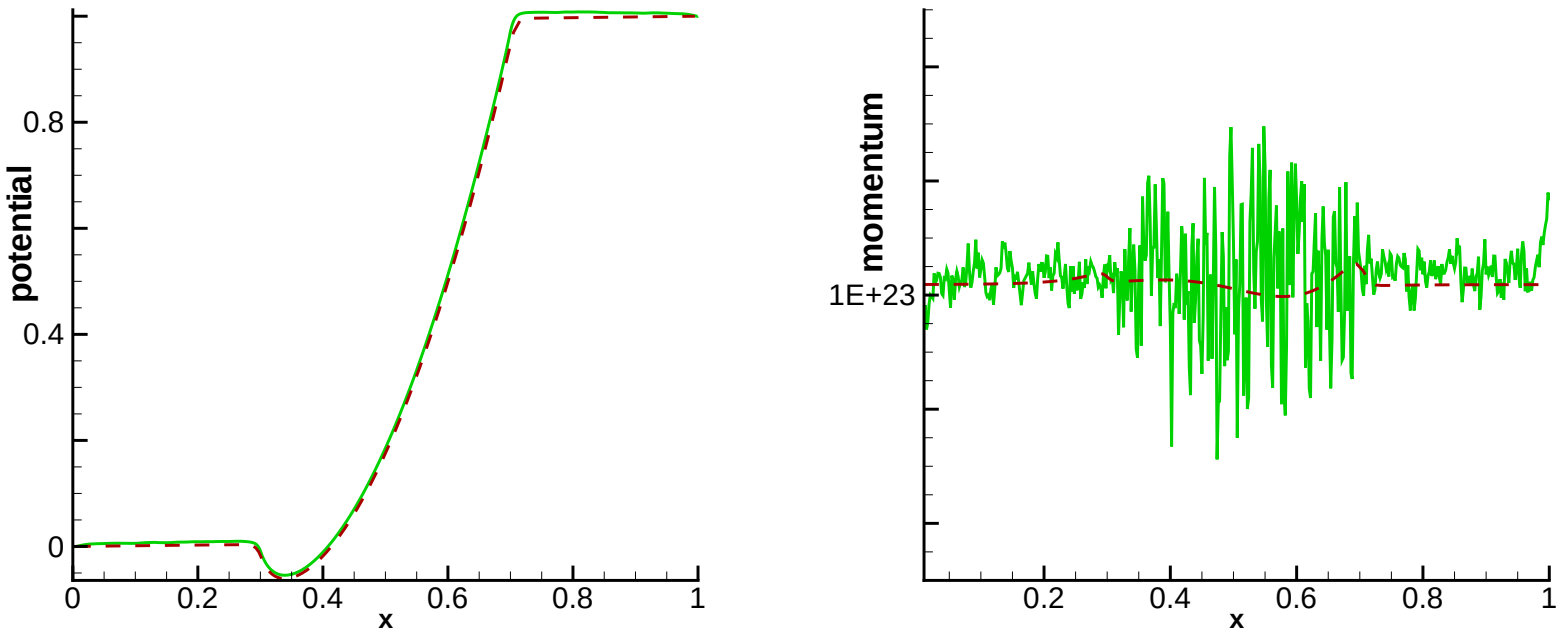

Figure 33: Comparison of macroscopic quantities using DG (dashed line) and DSMC (solid line) for 400nm channel at $t = 5.0$, $V_{\text{bias}} = 1.0$. Left: potential in V; right: momentum in $cm^{-2}\ s^{-1}$. Solution has reached steady state.

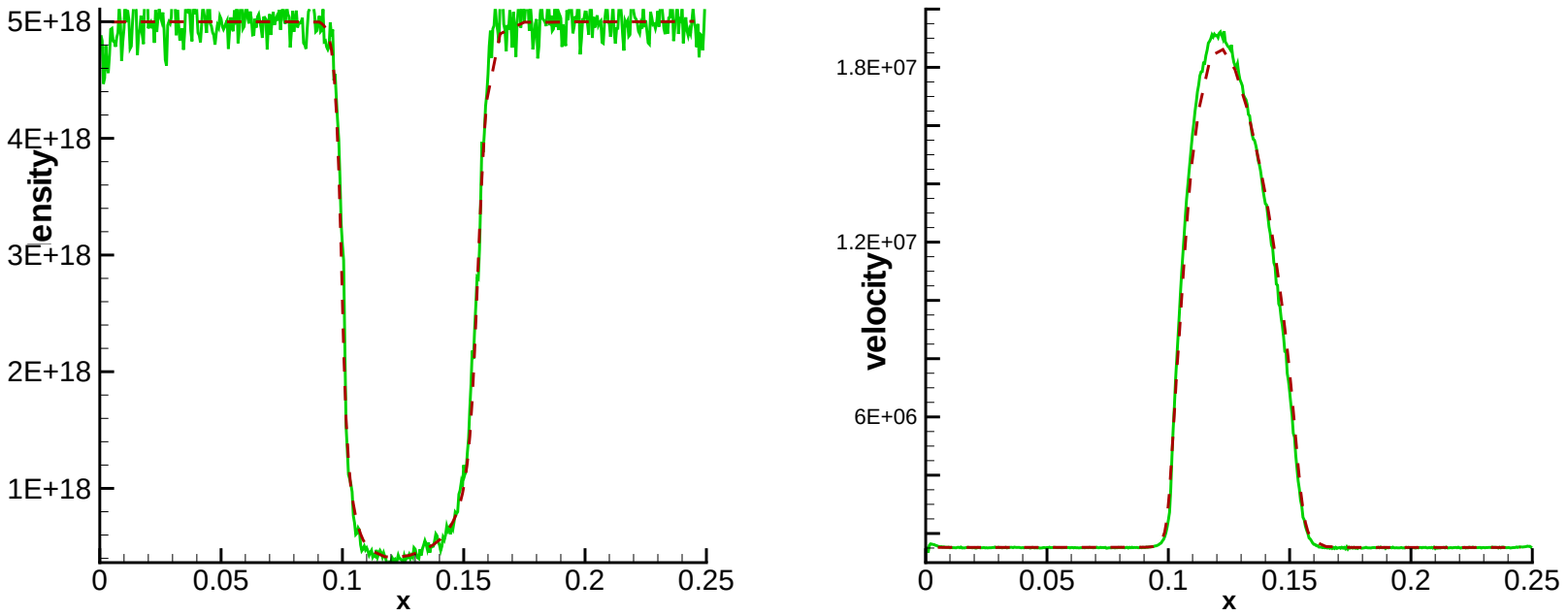

Figure 34: Comparison of macroscopic quantities using DG (dashed line) and DSMC (solid line) for 50nm channel at $t = 3.0$, $V_{\text{bias}} = 1.0$. Left: density in cm^{-3}; right: mean velocity in cm/s. Solution has reached steady state.

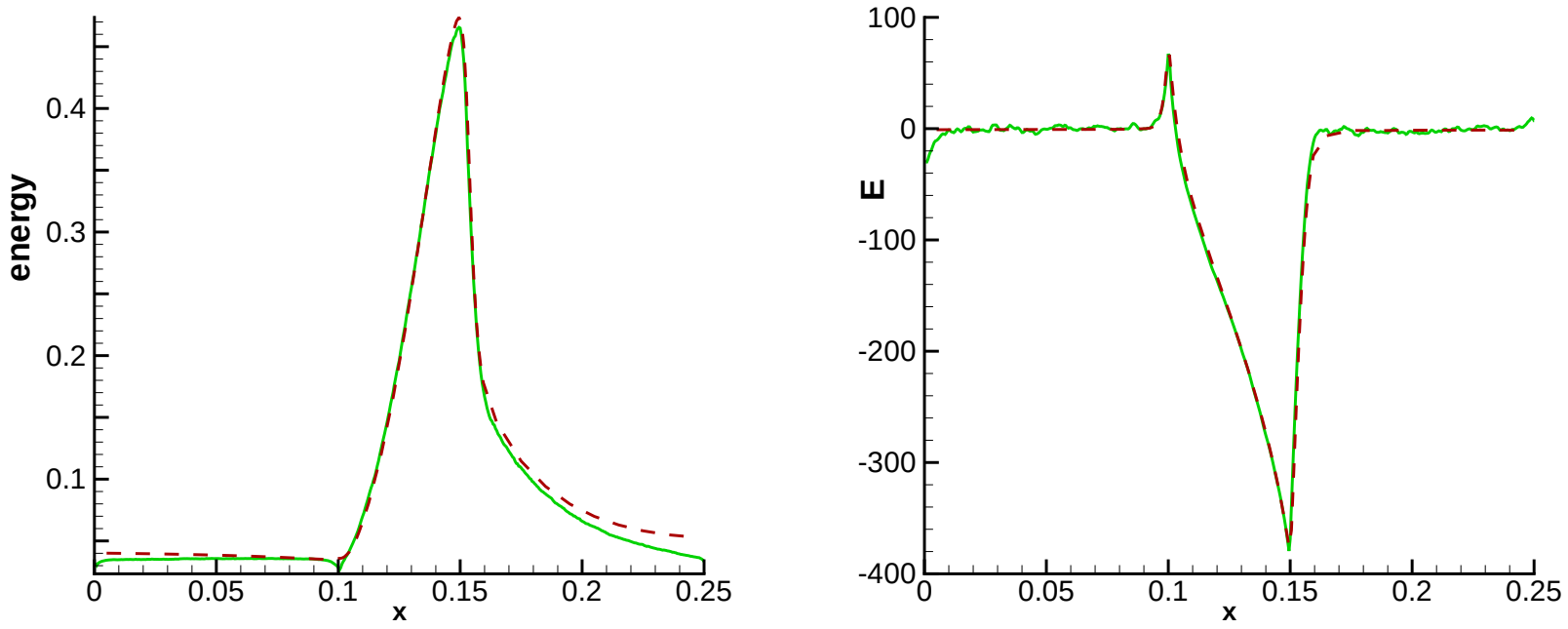

Figure 35: Comparison of macroscopic quantities using DG (dashed line) and DSMC (solid line) for 50nm channel at $t = 3.0$, $V_{\text{bias}} = 1.0$. Left: energy in eV; right: electric field in kV/cm. Solution has reached steady state.

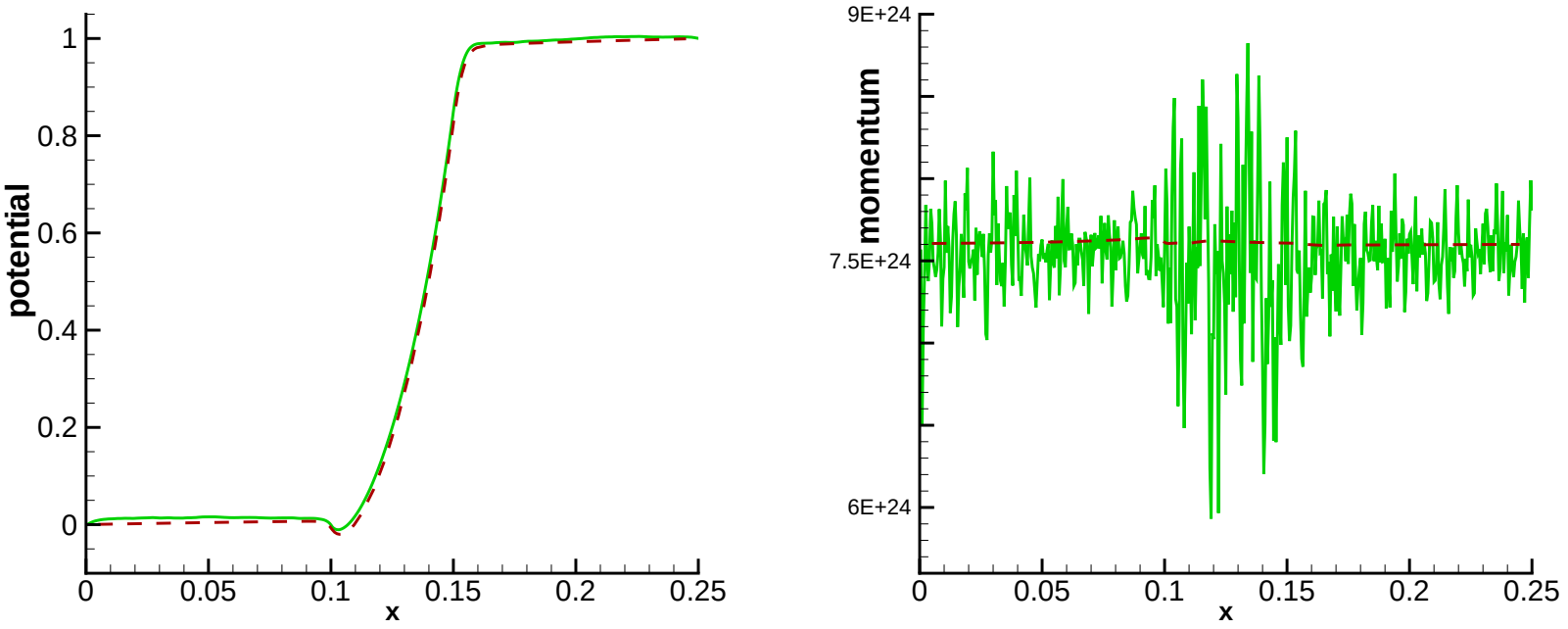

Figure 36: Comparison of macroscopic quantities using DG (dashed line) and DSMC (solid line) for 50nm channel at $t = 3.0$, $V_{\text{bias}} = 1.0$. Left: potential in V; right: momentum in $cm^{-2}\ s^{-1}$. Solution has reached steady state.

Next, we consider a 2D double gate MOSFET device.

The schematic plot of the double gate MOSFET device is given in the next figure. The shadowed region denotes the oxide-silicon region, whereas the rest is the silicon region.

For the Poisson equation, $\Psi = 0.52354$ at source, $\Psi = 1.5235$ at drain and $\Psi = 1.06$ at gate. For the rest of boundaries, we impose homogeneous Neumann boundary condition, i.e., $\frac{\partial \Psi}{\partial n} = 0$. The relative dielectric constant in the oxide-silicon region is $\epsilon_r = 3.9$, in the silicon region is $\epsilon_r = 11.7$.

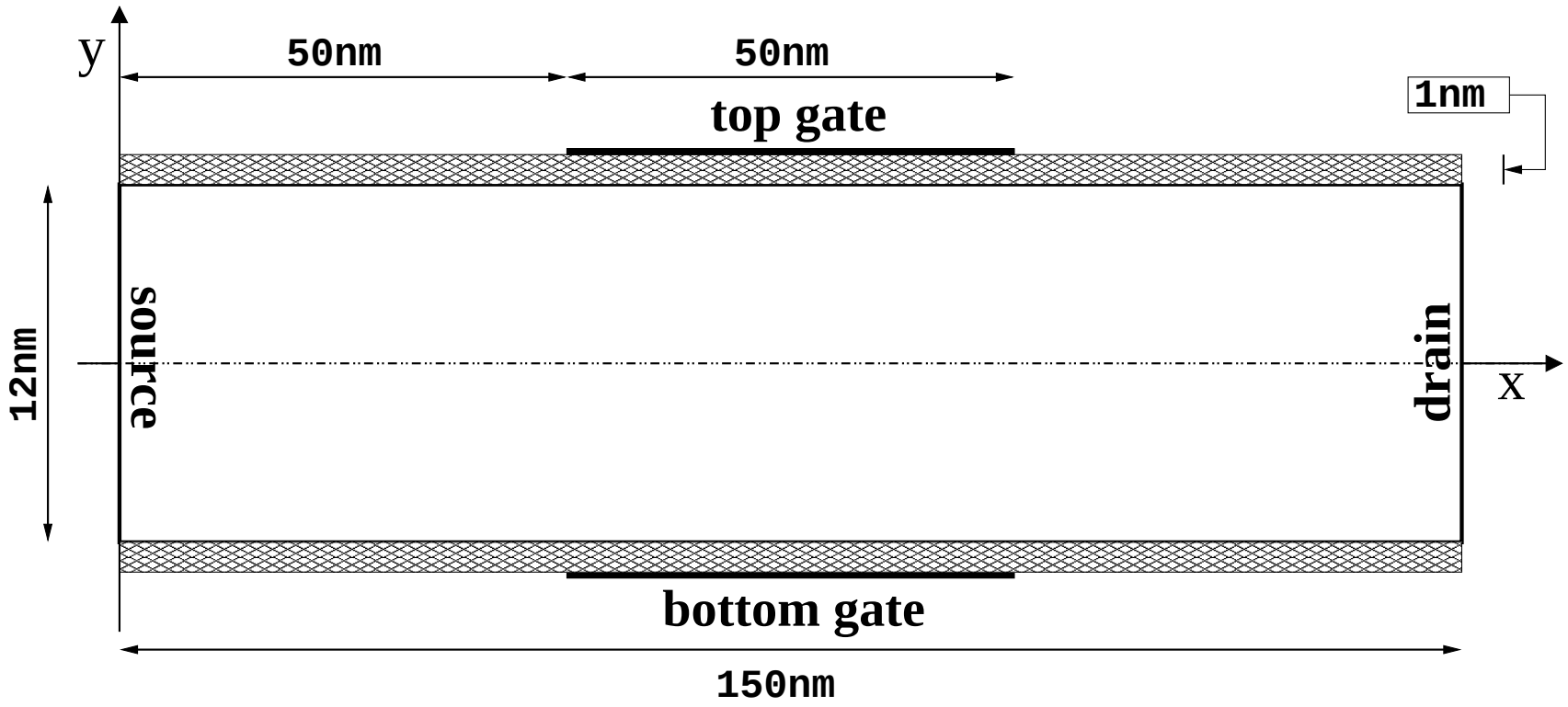

Figure 37: Schematic representation of a 2D double gate MOSFET device

All numerical results are obtained with a piecewise linear approximation space and first order Euler time stepping. Apparently the collision term makes the Euler forward time stepping stable. We use a 24×14 grid in space, 120 points in w, 8 points in μ and 6 points in φ. In the next figures, we show the results of the macroscopic quantities.

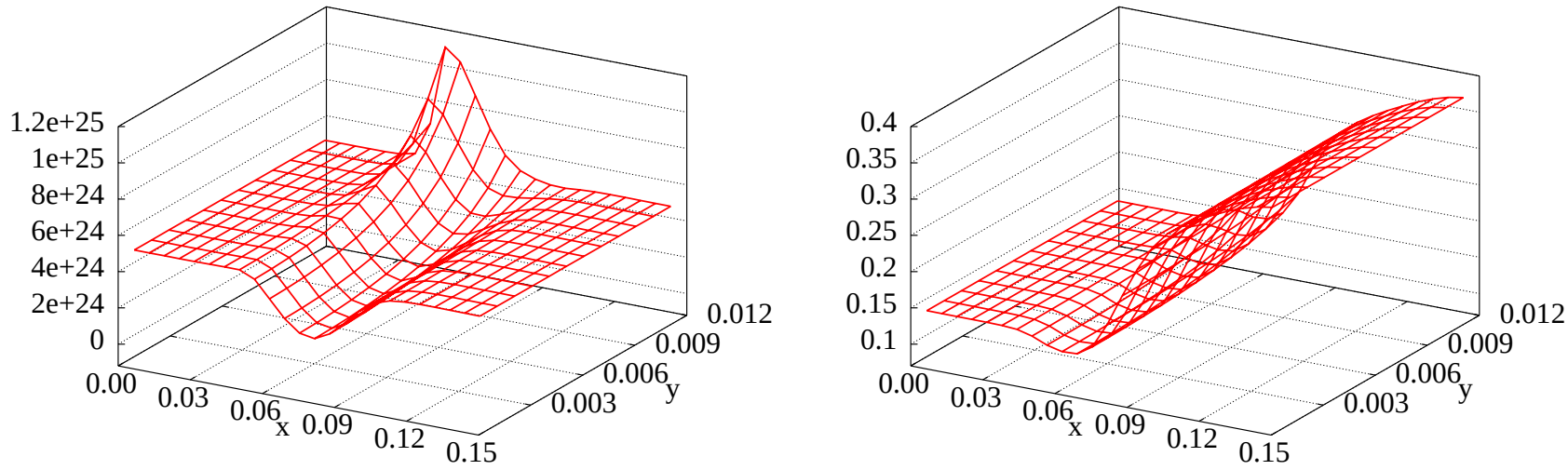

Figure 38: Macroscopic quantities of double gate MOSFET device at $t = 0.5$. Left: density in cm^{-3}; right: energy in eV. Solution reached steady state.

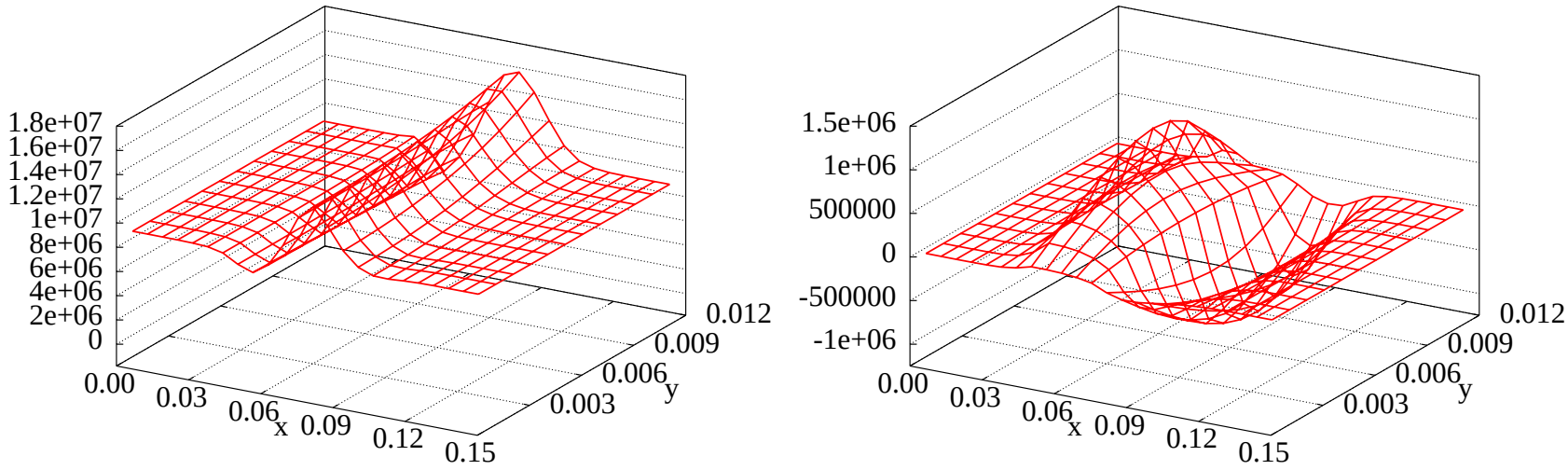

Figure 39: Macroscopic quantities of double gate MOSFET device at $t = 0.5$. Left: x-component of velocity in cm/s; right: y-component of velocity in cm/s. Solution reached steady state.

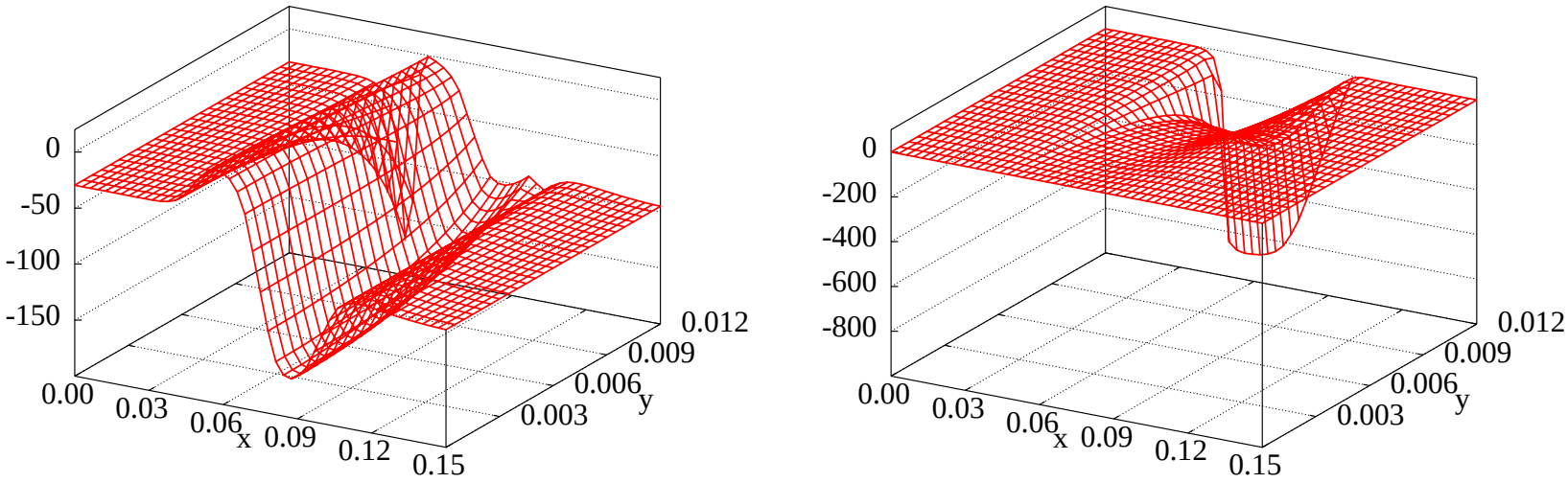

Figure 40: Macroscopic quantities of double gate MOSFET device at $t = 0.5$. Left: x-component of electric field in kV/cm; right: y-component of electric field in kV/cm. Solution has reached steady state.

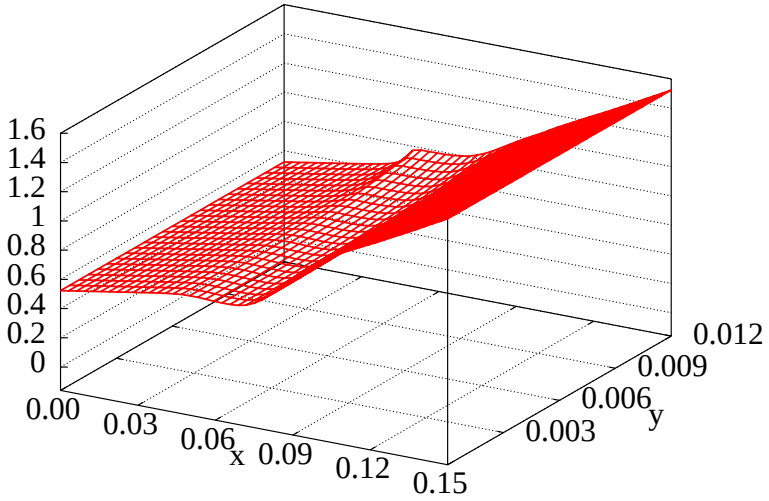

Figure 41: Macroscopic quantities of double gate MOSFET device at $t = 0.5$. Electric potential in V. Solution has reached steady state.

We also show the *pdf* at six different locations in the device in the next figures. These *pdf*'s have been computed by averaging the values of Φ_h over φ.

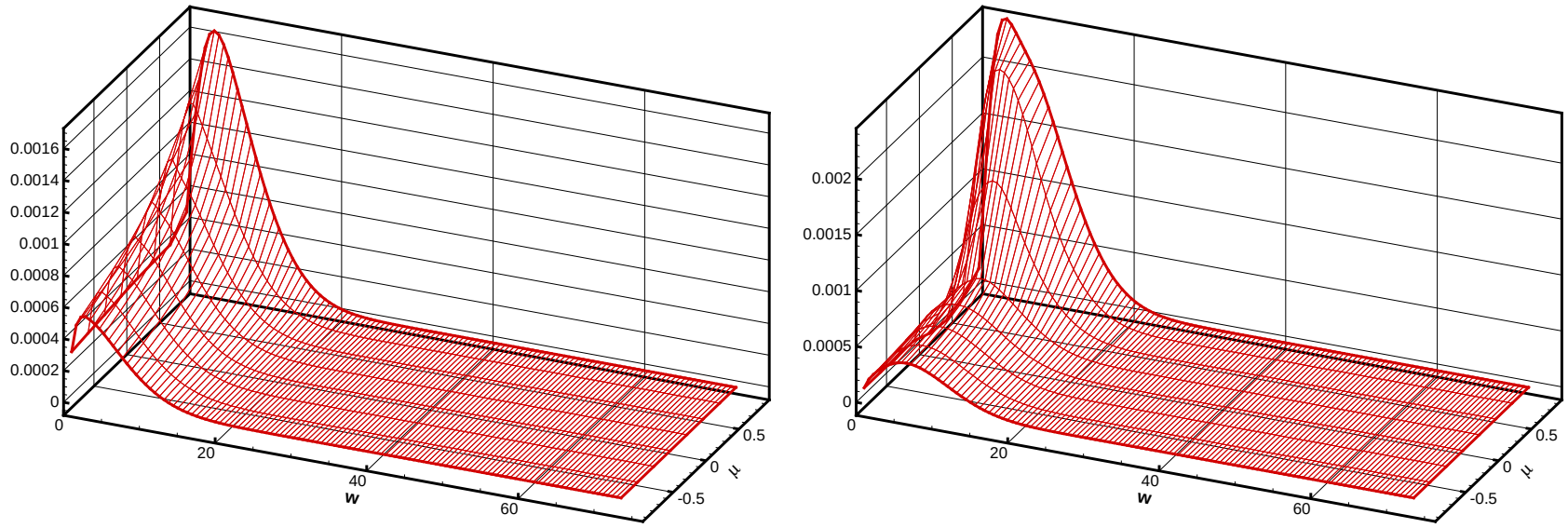

Figure 42: PDF of double gate MOSFET device at $t = 0.5$. Left: at (0.025, 0.12); right: at at (0.075, 0.12). Solution reached steady state.

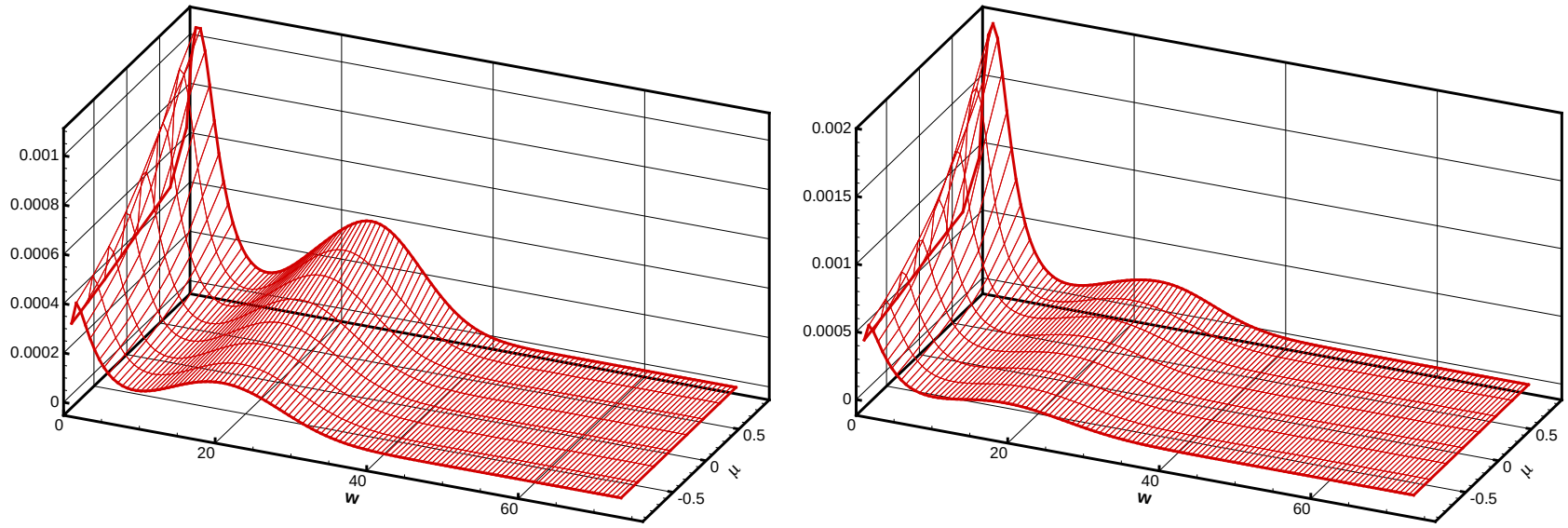

Figure 43: PDF of double gate MOSFET device at $t = 0.5$. Left: at (0.125, 0.12); right: at (0.1375, 0.06). Solution reached steady state.

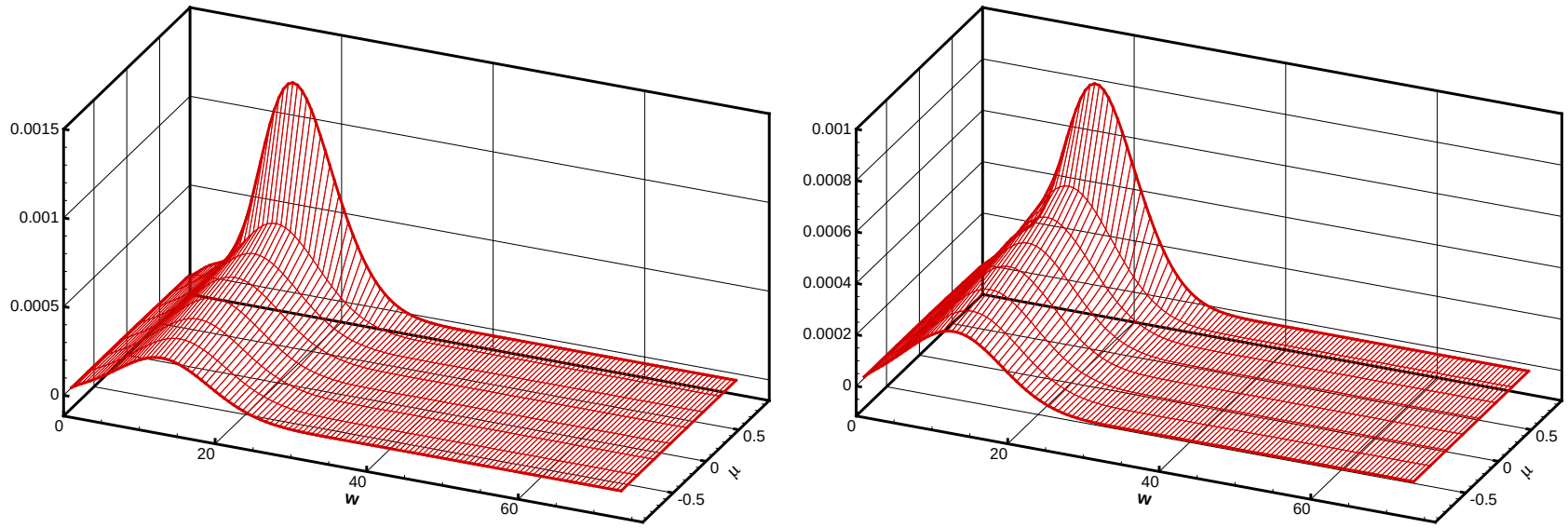

Figure 44: PDF of double gate MOSFET device at $t = 0.5$. Left: at (0.09375, 0.10); right: at (0.09375, 0.). Solution reached steady state.

In the next figure, we present the cartesian plot for *pdf* at $(x, y) = (0.125, 0.12)$, where a very non-equilibrium *pdf* is observed.

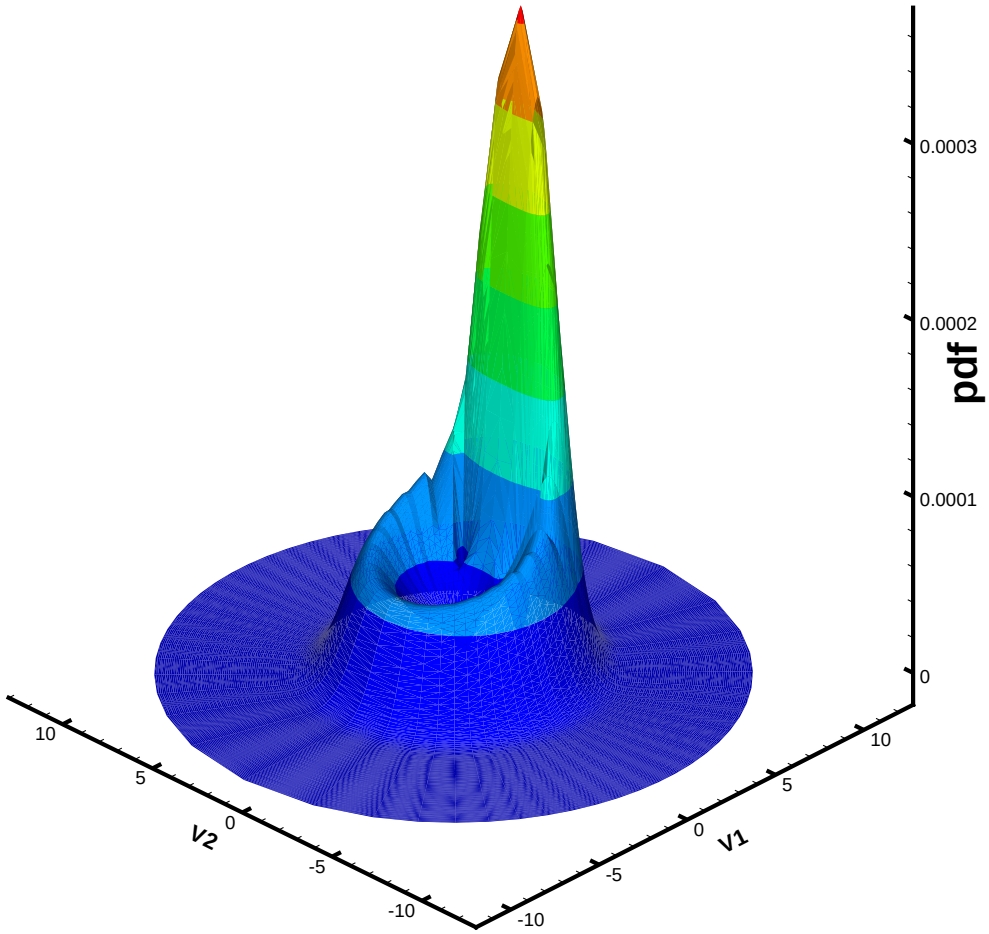

Figure 45: PDF for 2D double gate MOSFET at $t = 0.5$, $(x, y) = (0.9375, 0.10)$.

Conclusions and future work

We have implemented a DG method for solving the BP system up to 5 dimensions plus time.

Future work:

- Two band models
- More general collision
- Energy $\varepsilon(\mathbf{k})$ from a look-up table
- Adaptivity (both h and p)
- Other applications (than semiconductor)

The End

THANK YOU!